Multiscale Investigation of Freeze Cast Process and Ion Transport for Graphene Aerogel Electrodes

A Dissertation Presented for the

Doctor of Philosophy

Degree

The University of Tennessee, Knoxville

Yu-Kai Weng

December 2022

ACKNOWLEDGEMENTS

First, I would like to appreciate my family, my father, mother, and sister, for their unconditional love and support.

Besides my family, I would like to express my sincere gratitude to my advisor Prof. Seungha Shin, who always provided me with selfless support and immense knowledge during my Ph.D. research and dissertation writing. His kindness, patience, and motivation also help me to have a more successful future career. He is also a great mentor in my personal life. I could not have today's accomplishment without his training and guidance.

I would also like to thank the rest of my Ph.D. committee: Prof. David J. Keffer, Prof. Kenneth D. Kihm, and Prof. Douglas S. Aaron, for their insightful comments and encouragement during my research.

Last but not least, I want to thank my colleagues, including Ali Yousefzadi Nobakht, Drew C. Marable, Jiaqi Wang, Md Abdullah Al Hasan, and Wenyuan Zhu, for their support and encouragement.

Special thanks to all the friends and people I met these years. I could not have become a better person without you.

ABSTRACT

Effective use of renewable energy resources has been regarded as the most promising solution to climate emergency and energy crisis. However, the fluctuating and intermittent nature of renewable resources causes stability issues in the electric grid. High-capacity electrical energy storage is essential to stabilize the electric power supply using renewable resources. Among various types of energy storage systems, organic redox flow battery (ORFB) has attracted attentions due to their high stability, flexibility, low cost, and environmental compatibility, but the performance of the ORFB still needs a significant improvement due to their low energy or current density. Specifically, even though the efficiency of the electrode, where the redox reactions occur, is critical to the ORFB performance, the disordered structures of widely used carbon-based electrodes hinder the convective flux of electrolytes. This makes the ion transport through the electrodes very restricted, which is a major challenge in ORFB.

To overcome the major challenge while enhancing or maintaining other electrode properties, directional graphene aerogel (DGA) was proposed as an electrode material, and the DGA synthesis and ion transport for its electrode application are discussed here. As DGAs are synthesized by freeze casting, the control of water-ice phase change and the effect of graphene-water interaction on freezing and structuring are important to develop the DGA synthesis. Also, understanding of ion transport through graphene channels with convective flux should be enhanced for the design of effective DGA electrodes.

Multiscale simulations employing molecular dynamics and finite volume methods were conducted to investigate the propagation and shape of the water-ice interface under various freezing conditions (e.g., temperature, crystal orientation, container geometry, etc.) and the ion electric mobility with convective flux under different graphene-surface interactions and channel conditions. Through this research, I identified 1) various ice propagation control methods and structuring mechanisms during the freezing, 2) the roles of the Rayleigh-Bénard convection on the propagation and shape of the water-ice interface, and 3) the effects of surface interaction on the ion mobility in graphene nanochannels under the coupling of field- and pressure-driven transport. This research explores new possibilities to enhance the ion transport of DGA electrodes for ORFB.

TABLE OF CONTENTS

LIST OF TABLES

LIST OF FIGURES

Chapter 1
Introduction

1.1 Background: Organic Redox Flow Battery and Graphene Electrodes

Reducing the environmental impact of conventional electric energy generation from burning fossil fuels has undoubtedly become one of the most challenging global issues in the 21st century. Under these circumstances, the demand for power generation from renewable energy sources, defined as the energy harvested from natural sources continually restored by nature [1], has significantly increased in recent decades, and its continued growth is undoubtedly expected. However, compared with conventional energy sources, renewable energy, such as wind, solar, and hydropower, has an inevitable fluctuating and intermittent nature [2]. The unsteady electricity production from renewable sources would cause unnecessary loading or damage to the electric grid systems [3], hindering their broader application. To mitigate this unsteady electricity production problem and thus accommodate the increasing demand for renewable energy, the development of a massive energy storage system is critically necessary.

Among various energy storage technologies, the redox flow battery (RFB) has been recognized as a promising candidate for storing electronic power generated by renewable energy due to its expandable capacity, design flexibility, and operation safety [4-7]. The

RFB utilizes the chemical oxidation and reduction reactions to convert and store the electric energy in the liquid electrolytes solutions that flow through the battery cells [8]. In the company of several variations of the RFBs, the one using vanadium ion solution as the electrolyte has the advantages of a longer lifecycle and higher efficiency. These advantages make the vanadium redox flow battery (VRFB) has become the most popular type of RFB [9] in the industry. Nevertheless, the relatively high toxicity of VRFB is still a problematic issue [10] that prevents from broadening the possible application of RFBs. To facilitate the environmental and sociopolitical impact of the metal-based VRFB, an organic redox flow battery (ORFB) employing redox-active organic materials has been suggested.

The ORFB offers several advantages for electric energy storage (EES) systems. First, raw materials of ORFB can be acquired at a lower cost than the metallic precursor, which makes the ORFB have a higher potential to meet the cost target for large-scale ESS from ($100/kWh) from the United States Department of Energy (DoE) [5], and through the structural modifications and functionalization of the materials, the thermochemical properties of the electrode can be tuned [11]. Also, nonflammable organic electrolytes provide safety benefits for the EES system [12]. However, various disadvantages and drawbacks still need to be addressed for ORFB. One of the most reported challenges for ORFB is a relatively limited life cycle due to the electrochemical instability of organic electrolyte materials [1]. In addition, the low charge/discharge current density is also being recognized as another obstacle to the development of the ORFB [13]. To further improve the performance of the RFB, comprehensive studies of the component design and materials selection have been reported [14-17]. As a component that provides the active surface to

occur the electrochemical redox reactions, there is no doubt that the electrodes play a critical role in the RFBs. Therefore, the material of the electrodes on RFBs must have good electrochemical properties, such as ion transport efficiency, in addition to outstanding electrical conductivity and mechanical stability.

1.2 Motivations and Objectives

Several types of graphene-based material have been used as electrodes for RFBs, such as graphite felt or carbon felt [18-20], due to their high electrical conductivity, chemical stability, and larger surface area [21]. Even though these felt-type electrodes offer a great surface area and electrical conductivity for the redox couples in the electrolytes, the disordered and complex structure delays the flow of the electrolyte. Subsequently, the ion transport through the electrode is suppressed by the low-speed electrolyte flow, and overall energy efficiency is impacted. Thus, to improve the energy efficiency of the ORFB, the performance enhancements of graphene electrodes with effective ion transport based on the enhanced understanding of synthesis and ion transport process are necessary.

In this dissertation, two majority approaches are presented to improve the ion transport properties of the graphene electrodes. First, the electrolyte flow speed increment is attempted by enhancing the structural alignment of the graphene electrode. For this reason, the freeze casting process is introduced. Freeze casting is a production process that utilizes the directional phase-changing nature of the water inside the predefined container to produce the porous structure from the casting materials [22]. Once the alignment of the electrode structure is increased, the convective flux of the electrolyte can be efficiently

transported through the electrode. Therefore, the innovative directional graphene aerogel (DGA) is proposed as a material for the electrode on ORFB. Since the final structure of casting materials is determined by the water freezing behavior, such as the interface propagation speed, it is critical to have a fundamental knowledge of the interaction between the water-ice interface and graphene. Thus, the water-ice interface propagation effect on the graphene structuring during the freeze casting (directional freezing) needs comprehensive exanimation.

Additionally, the surface interaction of graphene has been reported that can be modified to change the behavior with the different particles [23]. Inspired by surface modification, the second approach is modifying the surface interaction between graphene walls and ions in the graphene electrodes. By doing so, the resistance of the ion transport through the electrode structure is expected to be controlled. Therefore, detailed knowledge of the surface interaction of graphene during ion transport is necessary.

In summary, the overarching goal of this dissertation is to enhance the fundamental understanding of graphene structuring and the ion transport process. The development of DGA electrodes with effective ion transport by freeze casting can be further advanced by the findings from this research. Ultimately, the performance of the ORFB could benefit from the findings of this work.

1.3 Research Overview

In this research, multi-scale numerical simulation is applied as the primary tool to produce and analyze the result. Since the freeze casting relies on the phase change process of the water to form the porous structure, the water-ice interface propagation becomes one of the critical factors in the synthesis of the DGA. Thus, the microscale water freezing, and graphene structuring are examined by conducting the molecular dynamics (MD) simulation. The propagation properties of the water-ice interface at various operating conditions are investigated. Moreover, the interaction effect between the crystal structure of the ice and the graphene surface is discussed based on the result from the MD simulation. On the other hand, since the Rayleigh-Bénard convection is a macroscale flow motion driven by the temperature gradient of the water [24], the final structure of the graphene aerogel can be affected by Rayleigh-Bénard convection during the freeze casting. The macroscale computational fluid dynamics (CFD) simulation is applied to investigate the Rayleigh-Bénard convection effect on the water-ice interface propagation during the freeze casting. In addition to the microscale water freezing and graphene structuring, the surface interaction effect on the ion transport through the graphene nanochannel with convective flux is also studied using MD simulation. Through this study, the role of surface interaction of the graphene structure in ion transport under various operating conditions is expected to be elucidated.

Figure 1.1 shows the overview of this research, which covered the following three topics:

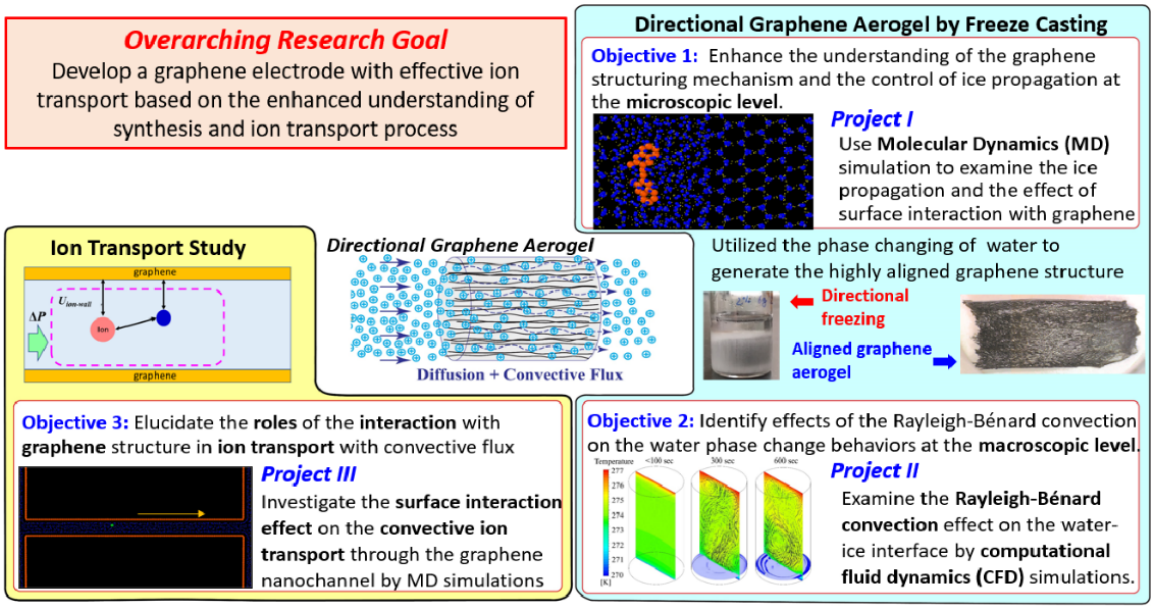

Figure 1.1 Overview of three research projects in this dissertation.

a) Understanding of the graphene structuring mechanism and the control of ice propagation at the microscopic level,

b) effects of the Rayleigh-Bénard convection on the water phase change behaviors at the macroscopic level, and

c) roles of the interaction with graphene structure in ion transport with convective flux.

In this dissertation, Chapter 2 presents the microscopic mechanism of the water-ice interface propagation and surface interaction between the crystal structure of ice and graphene flakes. In Chapter 3, the effect of the Rayleigh-Bénard convection on the water-ice interface propagation during directional freezing is discussed. The surface interaction effect from the graphene to the ion transport process with the convective flux is examined in Chapter 4. Chapter 5 summarizes the conclusions from this research and possible future works.

Chapter 2
Investigation of Microscopic Mechanisms for Water-Ice Phase Change Propagation Control

2.1 Abstract

The influence of thermodynamic and structural conditions on water-ice phase change process was investigated with consideration of graphene-water surface interactions for fundamental understanding and effective control of freezing propagation. The phase change propagation as well as structural and energetic properties during the phase change were examined by analyzing atomic data from molecular dynamics simulations. The freezing propagation speed is affected by the competition between atomic mobility and thermodynamic driving force for phase change, which causes an optimal temperature for fast ice growth to appear at 252 K. In addition, the water-ice interfacial energy, which depends on the orientation of the water-contacting ice surface, changes interfacial structural stability and thus freezing propagation, i.e., a higher interfacial energy leads to a faster ice propagation. Therefore, we suggest that the water-ice phase change propagation can be controlled by adjusting the orientation of ice crystal. The surface interactions, or graphene-water interactions in this research, affect the energetics near the water-surface interface. The energetic change rearranges the ice crystal or surface structures to reach the most stable ice-surface configuration or minimum energy state, in which the basal plane of the ice crystal is parallel with the graphene surface. As ice propagation is the slowest perpendicular to the basal plane, ice can grow faster parallel to graphene surface. The findings from this study provide insights to ice propagation control mechanisms for versatile freeze casting and its broader applications.

2.2 Disclosure

Chapter 2 is a modification of the published work: **Yu-Kai Weng**, Seungha Shin*, Kenneth D. Kihm, Mohammad Bahzad, and Douglas S. Aaron, "Investigation of Microscopic Mechanisms for Water-Ice Phase Change Propagation Control", International Journal of Heat and Mass Transfer, 184, 122357 (2022). This publication is reprinted with permission from Elsevier. The dissertation author listed in this publication directed and supervised the research which forms the basis for this publication.

2.3 Introduction

Water freezing is one of the most familiar phase-change phenomena in nature and an essential process for diverse science and engineering fields, such as microbiology [25], physics [26], and materials science [27]. One of the representative applications, which take advantage of the water-ice phase change process, is freeze casting or ice templating, where materials dispersed in liquid can be aligned by the anisotropic solidification of the liquid [28]. Freeze casting is employed to produce aligned porous structure from various building blocks [29], such as ceramics [30], graphene [31], and carbon nanotubes [32]. We studied the freezing process with an interest in the synthesis of graphene aerogels with aligned pores, which can be used as a component of electrochemical storage systems, specifically as an electrode material in organic redox flow batteries [33]. Since the working principle of freeze casting is to construct the material by phase change of water, water-ice interface propagation behaviors affect the resulting structure. For example, the average pore size and wall thickness of porous structures manufactured by freeze casting can be controlled by the

solidification velocity [34]. Therefore, investigation of effective control of ice front propagation is essential for the control of freeze-cast material structures and ultimately their application performance.

Previous studies reported that the thermodynamic driving force for phase change and the self-diffusivity of water molecules have an opposite dependency on the temperature in the supercooling region [35, 36]. Thus, temperature can be one of the parameters controlling ice growth rate [37]. Surface interaction can be another possible parameter to control ice propagation, as it was reported to change the ice crystal structure in the proximity of surface/water interface [38], which can also alter the ice propagation and freeze-cast structures. For example, if a droplet of water was frozen between two layers of graphene, a two-dimensional (2D) square-like crystal ice structure formed [39]. Since the interaction between water and graphene enhances the reordering of the water molecules [40], the freezing behavior and water-ice interface propagation near the graphene appear differently such as crystal structure [41]. Moreover, the average density profile and diffusion of water molecules near the interface can be changed by the crystal orientation of ice surface [42] in contact with water. Therefore, we can expect the control of water-ice interface propagation to be achieved by the surface interaction and ice crystal surface orientation at the interface as well as temperature.

Although water freezing behaviors have been studied for both pure water [35] and water-surface systems [43], the detailed mechanism of ice propagation and freeze casting process has not been identified clearly to the best of our knowledge. To find an effective control of ice propagation based on fundamental understanding of freezing process, we investigated

the water-ice phase change under various conditions, changing temperature, ice crystal orientation, and surface interaction. In this research, molecular dynamics (MD) simulations were employed to address the atomic-scale interactions and structures for the fundamental understanding. For the study of surface interaction, graphene was used as a surface material due to our interest in freeze casting of graphene aerogel for the development of electrode material with effective ion transport and its 2D nature that reduces computational cost and facilitates the analysis.

2.4 Methodology

Pure water structures were simulated via MD to examine the effects of temperature and ice crystalline structure (Fig. 2.1a), while the simulated systems for the study of surface interaction included graphene flakes or surface (Figs. 2.1b and 2.1c). Since the spontaneous ice nucleation from pure water requires a prohibitively large amount of simulation time in MD [44], a block of ice was introduced as a nucleation seed into initial simulation cells to accelerate the water-ice interface propagation. Here, initial structures of pure water and water with graphene flakes contain 50% of water molecules as ice, and a small ice seed is added near the graphene surface for water-graphene surface simulations. The periodic boundary conditions were used in all three dimensions. Therefore, in the simulation domain for a half-ice/half-water system, two water-ice interfaces (I_1 and I_2) exist, and they propagate in the opposite directions as in Fig. 2.1a. Simulations with graphene flakes (Fig. 2.1b) and those with ice cluster and a graphene plate (Fig. 2.1c) were conducted to investigate the effects of the surface-water interaction on the structural changes, i.e., re-

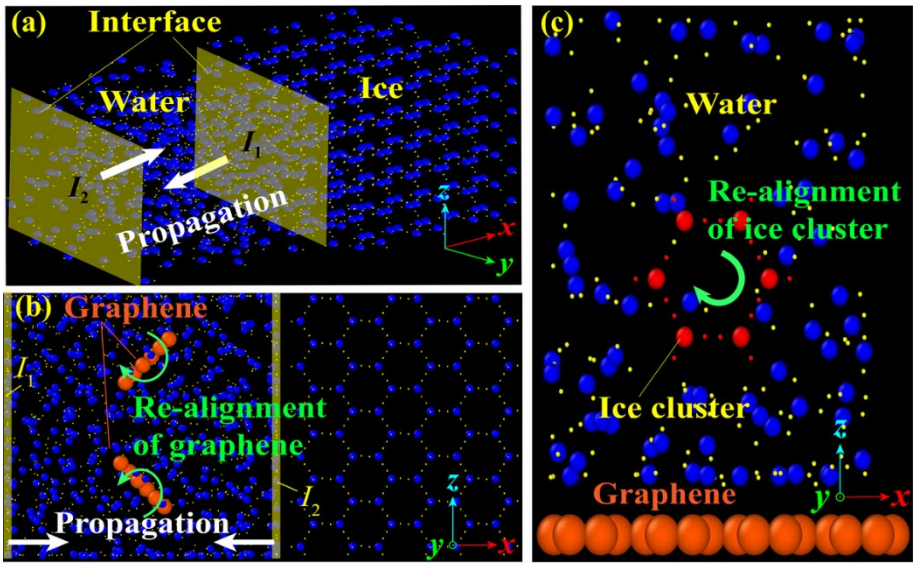

Figure 2.1 Initial atomic configurations of molecular dynamics simulations for (a) pure water freezing, (b) water freezing with movable graphene flakes, and (c) water freezing with a movable rigid ice cluster and a graphene plate at bottom. (Blue and yellow spheres: oxygen and hydrogen atoms from water or ice molecules, orange spheres: carbon atoms from graphene, and red spheres: oxygen and hydrogen atoms from the rigid ice cluster).

alignment of ice or graphene structure, during the ice propagation ultimately for enhanced understand of freeze casting.

The TIP4P/ICE model [45] was employed to calculate positions and momentums of water molecules because it accurately reproduces thermodynamic properties, especially ice-water phase change properties. TIP4P/ICE is a rigid water model that fixes bond length (O-H) of 9.572 Å and bond angle (H-O-H) of 104.52˚ as constant, and the charges of O and H atoms are -1.179e_c and 0.589e_c, respectively, where e_c is the elementary charge. The massless charge site M was introduced 0.1577 Å away from the O atom. The SHAKE algorithm [46] was also used to enforce the rigidity of water molecules. The particle-particle particle-mesh (PPPM) algorithm [47] is applied to compute the long-range coulombic interactions among the water molecules. In addition to the Coulombic interaction, dispersive intramolecular interactions (ϕ) between oxygen atoms of water molecules with a distance less than the cut-off distance (r_c) are calculated using the 12-6 Lennard-Jones (LJ) model [48]:

$$\phi(r) = 4\varepsilon\left[\left(\frac{\sigma}{r}\right)^{12} - \left(\frac{\sigma}{r}\right)^{6}\right], \quad r \le r_c, \tag{2.1}$$

where ε is the LJ interaction energy strength, σ is the distance at which the potential is zero, and r is the interatomic distance. In the simulations, the parameters for oxygen-oxygen interaction (O-O) were set as $\varepsilon_{o\text{-}o}$ = 9.142 meV, $\sigma_{o\text{-}o}$ = 3.16 Å, and $r_{c,o\text{-}o}$=8.5 Å. In the simulations including graphene, the carbon-oxygen (C-O) interaction for the graphene-water interaction was also calculated using a LJ model with parameters of $\varepsilon_{c\text{-}o}$ = 8.19 meV,

$\sigma_{c\text{-}o}$ = 3.19 Å, and $r_{c,c\text{-}o}$=8.0 Å [49]. The carbon-carbon (C-C) interaction within a graphene plate was modeled with the Tersoff potential [50].

To integrate Newton's equations of motion, the velocity-Verlet algorithm [51] was used, and the temperatures were controlled via Nose-Hoover thermostats in all MD simulations in this research. Pure water simulations used a time step of 1.0 fs, while simulations with graphene employed a shorter time step (0.5 fs) to treat carbon atoms with high vibrational frequencies. Two different sizes of water freezing simulations containing 864 and 9216 water molecules were conducted to verify the size effect on the simulation results. Moreover, since the triggering of the freezing process varies with surface-to-volume ratio [52], these two systems were adjusted to have the same ratio between the area of water-ice interface and the volume of ice. The result shows that the increment of propagation speed is relatively small (< 14%) with more than 10 times larger system size. This result is in a good agreement with a previous study [53].

In MD simulations, temperature, ice crystal orientation, and water-surface interaction were control parameters, and their effects on water-ice interface propagation were investigated. First, to examine the temperature dependence, a 52 Å × 21 Å × 27 Å water-ice system was initially equilibrated at 250 K with an *NPT* ensemble (i.e., fixed number of molecules, pressure, and temperature) for 3.5 ns. After initial relaxation, the ensemble was switched to *NVT* (constant number of molecules, volume, and temperature) at a desired temperature (*T*) ranging from 200 K to 270 K for 30 ns. The effect of ice crystal orientation was studied by simulating three cases of ice-water system with a different interface structure. Within a simulation box of 52 Å × 21 Å × 27 Å, the ice surface in contact with water has a crystal

structure of either basal plane, primary prism plane (denote as P1), or secondary prism plane (denote as P2) as depicted in Fig. 2.2a. For the analysis of ice propagation, we processed 20 ns of atomic data produced by MD simulations with *NVT* at 250 K, after the relaxation of the initial structures with different ice surface orientations for 1.0 ns (*NPT*, at 250 K).

For the study of the surface interaction, specifically graphene-water interaction, two types of MD simulations were performed. First, water-ice structures that included graphene flakes were used as initial structures to examine the structuring during the freezing process. Two graphene flakes were added to the half-water, half-ice system with a dimension of 52 Å × 21 Å × 27 Å. The distance between the centers of the graphene flakes was 13.3 Å and they have ±45˚ of inclination angles. Two different distances between the flakes and water-ice interface (d_{gi} = 3 and 14 Å) are set as Fig. 2.2b shows. The atomic data for analysis were recorded for 30 ns of a simulation with *NVT* at 220 K, and we examined the relative orientation between the graphene flakes and the basal plane of the ice crystal. The second case of freezing simulations with graphene-water interaction employed initial atomic structures of 17 Å × 17 Å × 22 Å water with a 17 Å × 17 Å graphene surface. A prebuilt ice seed of 4.5 Å × 5.2 Å × 4.6 Å was included, and the center of the ice seed was located 9.7 Å above the graphene surface. Three different crystal orientations of the ice seed surface (i.e., primary prism, secondary prism, and basal) facing the graphene were tested in MD as in Fig. 2.2c. The atomic trajectory data from the MD simulations (with *NVT* at 220 K) for 100 ns were used for the analysis of ice propagation and atomic behaviors during freezing. For the study of energetics during freezing, the regional energies of the three

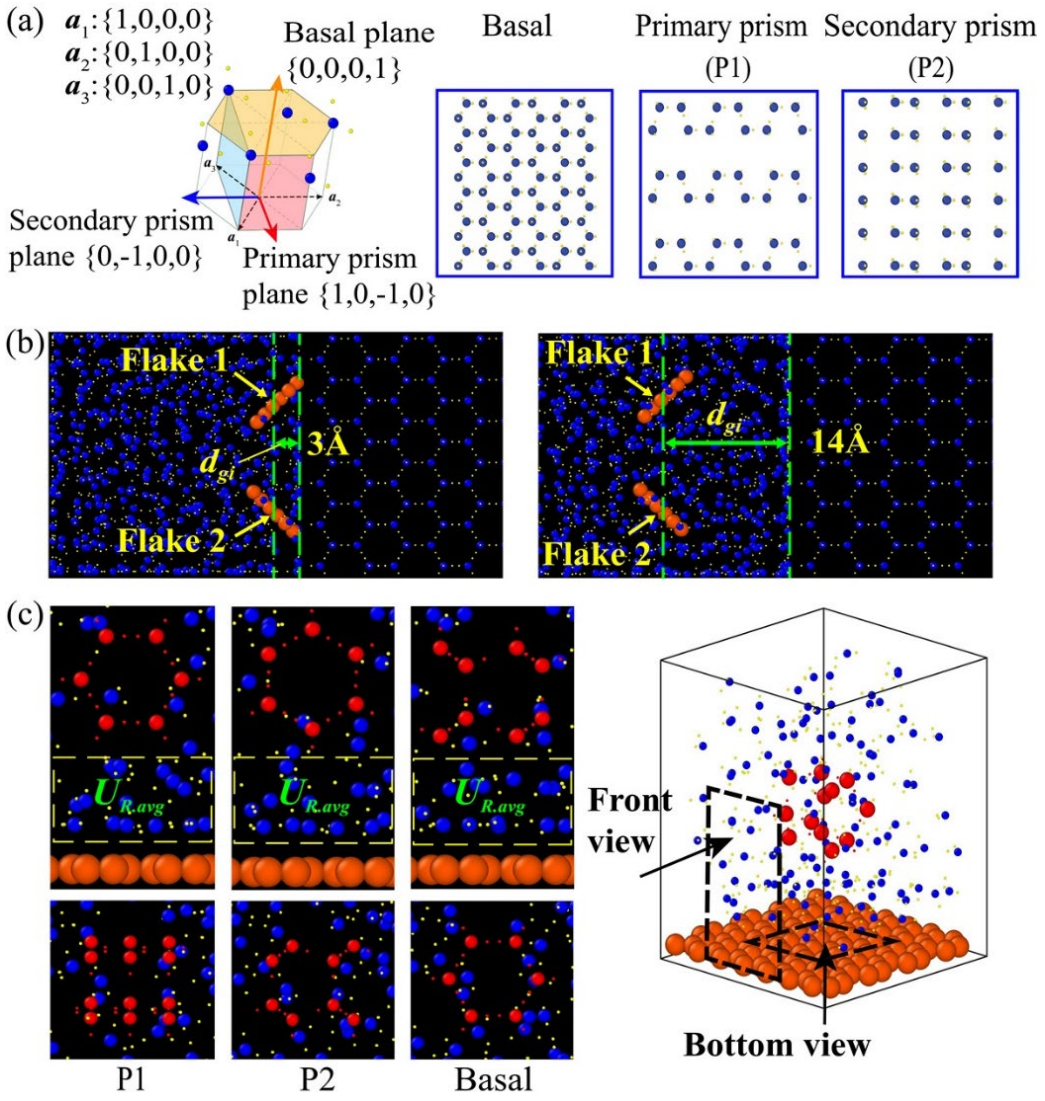

Figure 2.2 (a) Hexagonal ice crystal structure and basis vectors, and atomic configurations of three surface orientations (basal, primary prism, and secondary prism). (b) Initial atomic structures (oxygen: blue, hydrogen: yellow, and carbon: orange) of water-ice system with two inclined graphene flakes with two distances (d_{gi}) between the flakes and a water-ice interface, and (c) water with ice seed (red) on graphene surface (first row: front view and second row: bottom view). Three different surfaces of the ice crystals are facing down to graphene.

configurations ($U_{R.avg}$) were calculated from the potential energy of water molecules in the sampling region, which was defined between the ice cluster and graphene flakes (yellow dash line in Fig. 2.2c).

Since we studied effective control of ice propagation, the propagation speed was a major property that we measured by processing the resulting MD data. The speed was calculated using the location change of the water-ice interface with respect to time. To identify the phase (water or ice) and ultimately the location of the water-ice interface, we employed the Steinhardt-Nelson order parameter (q) [54]. This method quantitatively recognizes specific crystal orders based on spherical harmonic functions Y_{lm} [55], which are the solutions of the Laplace's equation in the spherical domains and widely used to describe spherical or near-spherical symmetry systems. Each Y_{lm}, where l and m stand for the orders of the functions, represents a specific shape of the solution. The Steinhardt-Nelson order parameter of order l of molecule i is given as,

$$q_l(i) = \sqrt{\frac{4\pi}{2l+1}\sum_{m=-l}^{+l}\left|q_{lm}(i)\right|^2}, \text{ where } q_{lm}(i) = \frac{1}{n_{NN}(i)}\sum_{j=1}^{n_{NN}(i)} Y_{lm}(\boldsymbol{r}_{ij}),\ j \neq i. \qquad (2.2)$$

Here, $\boldsymbol{r}_{ij}$ represents a position vector from molecule i to j (represented by O atom), and $n_{NN}(i)$ is the total number of the nearest neighboring molecules of i. Using the structure order parameters of molecule i and its nearest neighboring molecules, the average structure order parameter $\bar{q}_l(i)$ is calculated as [56]

$$\bar{q}_l(i) = \sqrt{\frac{4\pi}{2l+1}\sum_{m=-l}^{l}\left|\bar{q}_{lm}(i)\right|^2}, \text{ where } \bar{q}_{lm}(i) = \frac{1}{n_{NN}(i)+1}\sum_{j=1}^{n_{NN}(i)+1} q_{lm}(j). \qquad (2.3)$$

Water molecules with the average Steinhardt-Nelson parameter of order 6 larger than 0.385 ($\bar{q}_6 > 0.385$) are recognized as ice-like phase, while those with $\bar{q}_6 < 0.385$ are as water-like phase [56]. For ice-like structures ($\bar{q}_6 > 0.385$), $\bar{q}_4$ is used to identify a more detailed structure order; i.e., when $\bar{q}_4 < 0.42$, the ice structure is regarded as hexagonal (ice-I_h), while it is cubic for $\bar{q}_4 > 0.42$ (ice-I_c). Thus, the $\bar{q}_6$-$\bar{q}_4$ scatter plot was used to analyze the freezing progress and the detailed ice crystal structure. For the calculation of the water-ice interface propagation speed u_{wi}, the entire simulation domain of the water-ice system was subdivided into n slabs (S_k, k = 1, 2, 3, ..., n) with a uniform thickness of 4.2 Å along the x-axis (ice propagation direction). Local structure order parameter ($\bar{q}_{6,k}$) at $x = x_k$ (the center location of slab k) was evaluated by taking an ensemble average of $\bar{q}_6$ of water molecules in slab k. Using the spatial distribution of local structure order parameter $\bar{q}_{6,k}$ and the ice-water criterion for $\bar{q}_6$, the location of the water-ice interface was identified. Since the freezing propagation accelerates as the liquid volume shrinks, the calculation of u_{wi} excluded the freezing of the last two slabs before the freezing completion of the whole simulation domain.

To understand detailed mechanisms of ice propagation control, we examined the thermodynamic driving force of water-ice phase change, the mobility of water molecules to join the phase transition, and the interfacial energetics. These are characterized by calculating i) the difference of free energy between water and ice phases, ΔG (eV), ii) self-diffusivity of water molecules, D (m^2/s), and iii) water-ice interfacial energy γ_{wi} (mJ/m^2) [57], respectively. Using the free-energy perturbation (FEP) method [58], the free-energy difference (ΔG) between state A and state B was calculated as

$$\Delta_A^B G = -k_B T \ln \left\langle \exp(-\frac{U_B - U_A}{k_B T}) \right\rangle, \tag{2.4}$$

where k_B is Boltzmann's constant (8.617×10^{-5} eV/K), and U_A and U_B are the potential energies of the system at state A and state B, respectively, and the angle brackets represent an ensemble average. In MD, the free-energy perturbation is applied by coupling a perturbation parameter λ into the interaction force calculation, varying λ from 0 to 1 with an increment of $d\lambda = 0.001$. The perturbation parameter λ was introduced into the atomic point charges of oxygen and hydrogen atoms ($\lambda = 0$ for no charge, while $\lambda = 1$ for full charge). Therefore, the free energy (G) in this study was determined as overall free-energy difference $\Delta_{\lambda=0}^{\lambda=1} G$, which was obtained from the ensemble average (over 10,000 cases for each λ) of the free-energy difference from timestep i to i+1:

$$\Delta_{\lambda=0}^{\lambda=1} G = \sum_{i=0}^{n-1} \Delta_{\lambda_i}^{\lambda_{i+1}} G = -k_B T \sum_{i=0}^{n-1} \ln \left\langle \exp(-\frac{U_{i+1} - U_i}{k_B T}) \right\rangle_{\lambda_i}, \ i = 1 \cdots n, \tag{2.5}$$

where n is the total number of the timesteps during the simulation.

The self-diffusivity can be calculated by taking the mean square displacement (MSD) of the simulated molecules [59, 60]:

$$\mathrm{MSD}(t) = \left\langle \Delta \boldsymbol{r}(t)^2 \right\rangle = \frac{1}{N} \sum_{i=1}^{N} \left[\boldsymbol{r}_i(t) - \boldsymbol{r}_i(0) \right]^2, \tag{2.6}$$

where $\boldsymbol{r}_i(t)$ is the position vector of oxygen atom i at time t. Using the time dependence of MSD(t), the self-diffusivity (D) is given as,

$$D = \lim_{t \to \infty} \frac{\mathrm{MSD}(t)}{6t}. \tag{2.7}$$

With the calculated D, the diffusion activation energy of supercooled water can be obtained by fitting D with respect to temperature to the Arrhenius expression [61]:

$$D = D_0 \exp\left(-\frac{Q_v}{k_B T}\right), \tag{2.8}$$

where D_0 is pre-exponential factor, and Q_v is the activation energy (eV). To estimate the dependence of the diffusivity on temperature, a series of MD simulations of supercooled pure water systems (with 432 water molecules) were conducted at T = 200 – 270 K.

Unlike the free-energy difference and the diffusivity, the water/ice interfacial energy (γ_{wi}) is independent of temperature [62]. The calculation of γ_{wi} employed the ensemble switch method [63], where the energy difference between two different ensemble stages is calculated. In the first stage, two separate ice and water systems are simulated under the periodic boundary conditions in all directions. The total energies of ice-only and water-only simulation structures were measured under equilibrium and denoted as E_w and E_i, respectively. Then, combining the water and ice systems, the total energy E_{w+i} of the combined systems was calculated and compared with that from the separate systems. Therefore, the interfacial energy γ_{wi} is given by

$$\gamma_{wi} = \frac{E_{w+i} - (E_w + E_i)}{2A}, \tag{2.9}$$

where A is the area of water-ice interface.

2.5 Results and Discussion

2.5.1 Ice propagation in pure water

During freezing, new layers of crystal ice are formed near the water-ice interface until the entire system is frozen. As depicted in Fig. 2.3a, the water-ice interfaces (I_1 and I_2) were

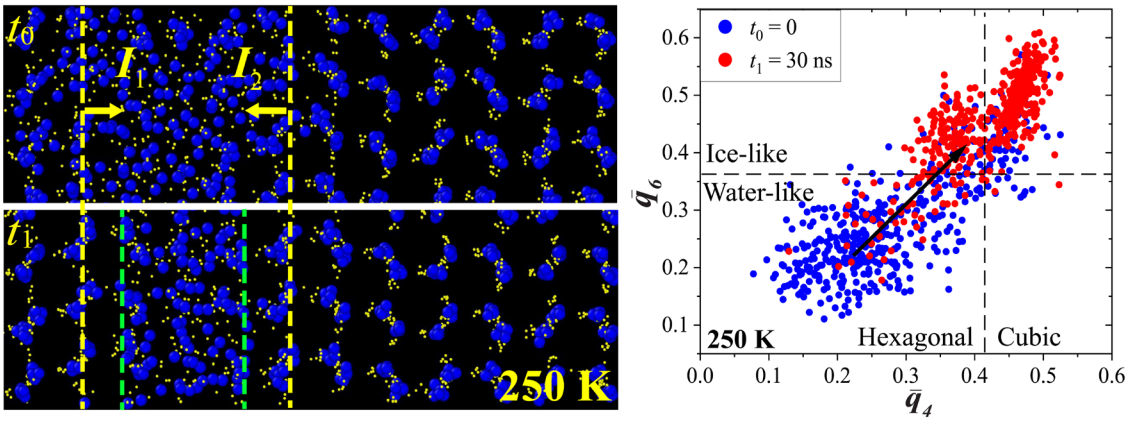

(a) (b)

Figure 2.3 The freezing process of water-ice system at 250 K: (a) the water-ice interfaces propagate from ice region toward water region, and (b) the structure order parameter plot at two different time steps, (t_0 = 0; t_1= 30 ns after freezing process). More molecules have structure order parameters $\bar{q}_6$ larger than the water-ice criterion of 0.385 at $t = t_1$, demonstrating the formation of hexagonal ice structure.

propagated, expanding the crystal ice region between 0 and 30 ns after relaxation. The scatter plot of structure order parameters of water molecules in the entire simulation domain quantitatively confirms the expansion of ice crystal (Fig. 2.3b), i.e., more data points or more molecules of local order parameter $\bar{q}_6 > 0.385$ at $t = 30$ ns.

To examine the water-ice propagation speed under different temperature below the freezing point of the system, the supercooling temperature is defined as $\Delta T_{sc} = T_m - T_{sys}$, where T_m is the water-ice phase change temperature in MD simulations (265 K in this study) and T_{sys} is the simulated system temperature. In pure water-ice systems, the water-ice interface propagation speed (u_{wi}), which was estimated by averaging the propagation speed from three crystal surfaces (P1, P2, and basal), reached the maximum (0.20 m/s) at 13 K of ΔT_{sc} (denoted as $\Delta T_{sc,max}$), as shown in Fig. 2.4a. When the supercooling temperature is lower than $\Delta T_{sc,max}$, u_{wi} decreased with decreasing ΔT_{sc}, while for $\Delta T_{sc} > \Delta T_{sc,max}$, u_{wi} increased with decreasing ΔT_{sc}. In the simulations, significant water-ice interface propagation (0.02 m/s to 0.20 m/s) was observed in the range of 3 – 25 K of ΔT_{sc}. The supercooling and the maximum propagation from our simulations (u_{wi} = 0.20 m/s at 13 K of ΔT_{sc}) are in good agreements with other MD works [35, 64] and experimental works [65], as presented in Fig. 2.4a. Even though the maximum propagation speed appears at larger ΔT_{sc} in the experimental work [65, 66], the overall dependence and speed are similar to our study.

The number of water molecules in an ice-like structure ($\bar{q}_6 > 0.385$) at 30 ns after the beginning of ice propagation was the largest at $\Delta T_{sc,\max}$ (= 13 K), while at 65 K of ΔT_{sc}, transition to ice structure in the initial water region was not observed (Fig. 2.4b).

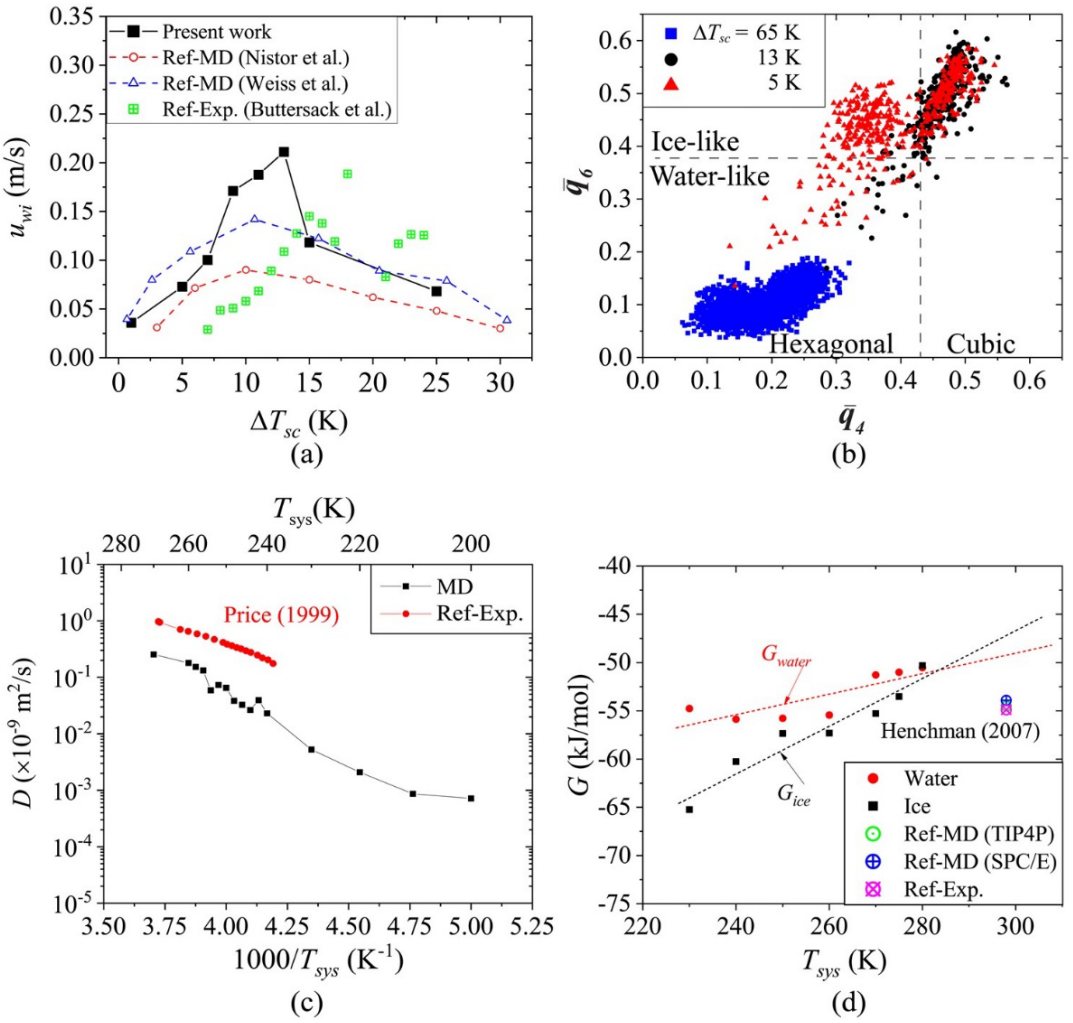

Figure 2.4 (a) The water-ice interface propagation speed (u_{wi}) averaged over three crystal orientations with respect to the supercooling temperature (ΔT_{sc}). The red open circles and blue open triangles represent the results of ice propagation speed from other MD studies [35, 64], and the green cross rectangles do those from a previous experimental study [65].

Large fraction of newly formed ice structures, when the highest propagation speed appears (i.e., at $\Delta T_{sc,\max}$ = 13 K), are cubic-like, while the hexagonal ice structures are created partially in case of ΔT_{sc} = 5 K with a lower propagation speed. This is attributed to a rapid phase transformation at $\Delta T_{sc,\max}$ which causes the metastable phase of ice (ice-I_c). On the other hand, the lower propagation speed provides water molecules with sufficient time for transition to more stable phase, i.e., hexagonal ice structure (ice-I_h) [67].

To explain the dependency of u_{wi} on the temperature (T_{sys}), the mobility of water molecules and thermodynamic driving force of water-ice phase change were examined by calculating the self-diffusivity D and the free-energy difference between water and ice (ΔG) at several temperatures. The self-diffusivity D describes the random translational movement of water molecules driven by the internal kinetic energy [68]. Figure 2.4c shows the self-diffusivity D of supercooled water calculated using MD data in a temperature range of 200 – 280 K, and the results are compared with experiments [69]. Although the self-diffusivities from MD are around five times smaller than the experiments, the MD activation energy (-35.82 kJ/mol) that was calculated from the temperature-dependence of the self-diffusivity between 200 K and 270 K is close to the value determined by the experiment (-30.16 kJ/mol) from 240 K to 270 K. The discrepancy from the experiments can originate from the size effect in molecular simulations or the usage of rigid water model, where atomic movements are constrained [70]. The appearance of the maximum u_{wi} at higher temperatures (smaller supercooling) in MD than experiments can be attributed to the lower of self-diffusivity in MD, as Fig. 2.4c presents. Since temperature represents the average kinetic energy of water molecules, lower temperatures lead to lower mobilities or smaller self-diffusivity. The

lower mobilities of water molecules slow the ice propagation as the transition to ice requires the migration of water molecules to a lattice point of the ice crystal.

While the mobility of water molecules increases with temperature, the thermodynamic driving force of the phase change, which we characterized using the free-energy difference between supercooled water and ice, decreases with increasing temperature, as Fig. 2.4d shows. Linear fitting and extrapolation of the free-energy values from MD simulations indicate that the free energy of crystal ice is less than that of water when $T_{sys} < 280$ K, which confirms that ice is more energetically stable. The opposite temperature dependencies of the thermodynamic driving force and self-diffusivity of water molecules explain the existence of optimum freezing temperature ($T_{wi,\max}$) for the maximum water-ice propagation speed (252 K in this report).

The water-ice interface propagation speed (u_{wi}) also depends on the orientation of ice crystal surface that contacts water as shown in Figs. 2.5a and 2.5b. When the secondary plane (P2) of ice crystal is in contact with liquid water, the water-ice interface propagation is the fastest in all ranges of ΔT_{sc} (Fig. 2.5a), while the basal plane-water interface has the slowest propagation speed. The energy analysis (Fig. 2.5b) also shows that a larger water-ice interfacial energy (γ_{wi}) was measured in case of faster propagation speed; P2-water interface has the largest γ_{wi}, and the basal plane-water interface has the lowest. Since a lower interfacial energy represents a more stable configuration, which leads to a lower atomic mobility and slower ice propagation [71], the dependence of freezing propagation speed on the water-ice interface orientation can be attributed to the interfacial energy.

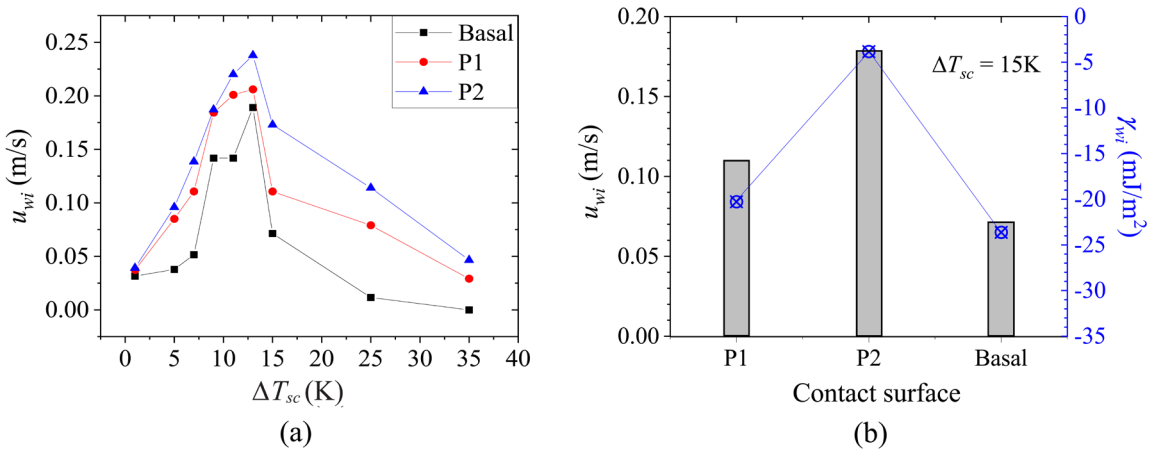

Figure 2.5 (a) Temperature dependency of propagation speed from different crystal orientations at interface. (b) Speed of water-ice interface propagation (u_{wi}; gray bars) and interfacial energy (γ_{wi}; blue crossed circles) for the three different orientations at 15 K of ΔT_{sc}.

2.5.2 Effects of water-graphene interaction

The effects of surface-water interactions on water phase change process, in addition to pure water properties discussed in Sec. 2.1, were examined for the understanding of freeze casting. In the freezing simulations of water with graphene flakes for the study of surface interaction effects, all the surfaces of graphene flakes were initially perpendicular to the basal plane of the ice crystal, i.e., angle between graphene and basal plane normal vector, θ_f is 90˚, as in Fig. 2.6a. However, due to the water-graphene interactions, as ice propagates near graphene surface, all the graphene flakes rotated about the long axis of the flakes, reducing the angles with the basal plane ($\theta_{f,1}$ and $\theta_{f,2}$, where 1 and 2 are index of the flake) as in Fig. 2.6b. The change of the angle between graphene flakes and the ice crystal basal plane are summarized in the Table 2.1 Two cases of the simulations with different distances between flakes and the water-ice interface (d_{gi} = 3 and 14 Å) show that the larger distance case resulted in the re-arrangement of two graphene flakes with more similar degrees of the flake-basal plane angle.

The preferred parallel angle between graphene surface and ice crystal basal plane was also observed in the simulations with a large graphene surface. Even with a different initial orientation of ice seed as described in Fig. 2.2c, the ice cluster ended up with the basal plane parallel to the graphene surface as shown in Figs. 2.7a and 2.7b. Thus, for the first two cases of initial ice cluster orientations, where a primary or secondary prism plane (P1 and P2) of ice cluster is parallel to the graphene surface, the ice cluster rotated to have the basal plane facing down.

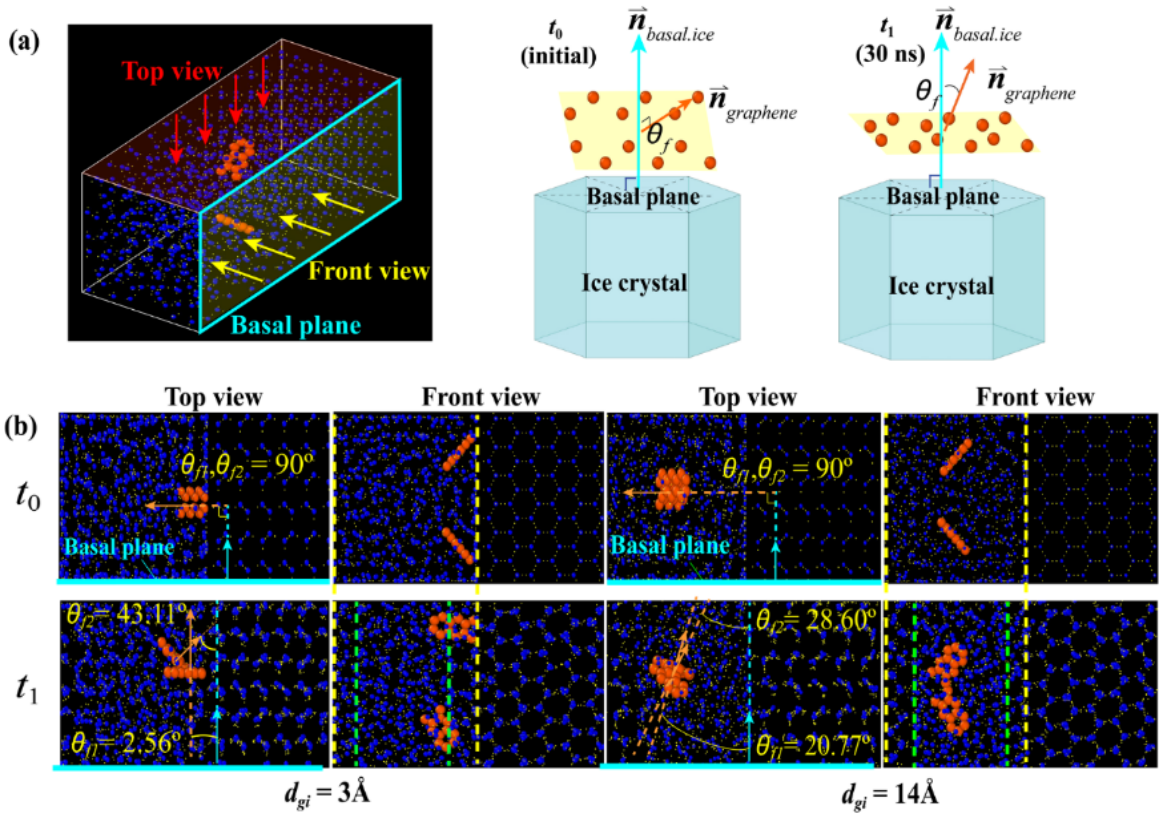

Figure 2.6 (a) Schematic illustration of the angle between graphene and basal plane normal vector. (Cyan surfaces and arrows: basal plane and its normal vector, orange arrows: normal vector of graphene flake surfaces) (b) Change of the alignment of two graphene flakes during the freezing process between $t_0 = 0$ and $t_1 = 30$ ns. The crystal surface of the interface is secondary prism plane (P2).

Table 2.1 Angles between the graphene flakes and the basal plane of ice crystal ($\theta_{f,1}$ and $\theta_{f,2}$) at $t_1 = 30$ ns for two different distances between the graphene flake and water-ice interface ($d_{gi} = 3$ and 14 Å).

d_{gi} (Å)	$\theta_{f,1}$	$\theta_{f,2}$
3	2.56 ˚	43.11˚
14	20.77˚	28.60˚

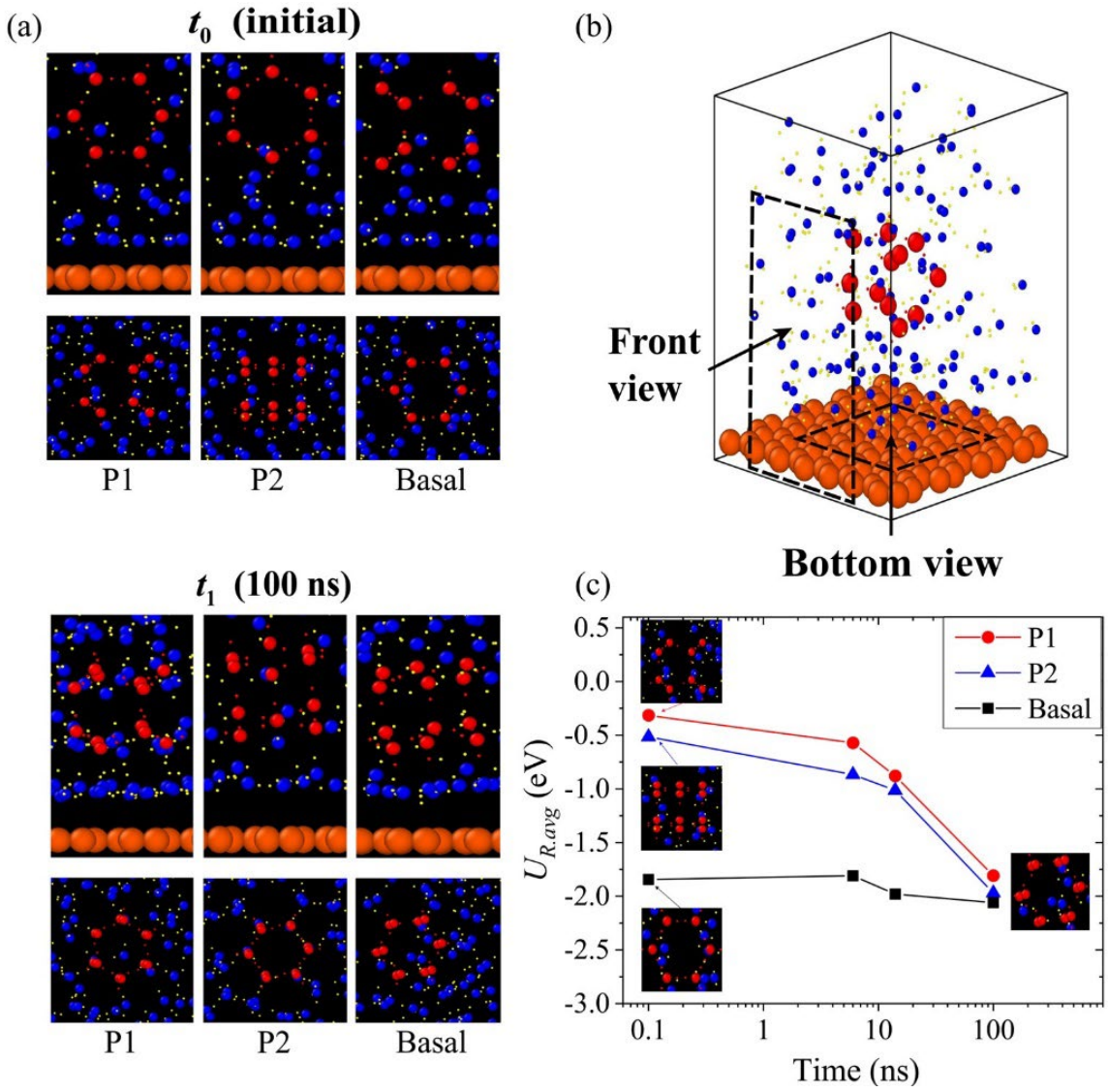

Figure 2.7 (a) Atomic configurations from the bottom view of water freezing simulations with graphene surface (orange) and three different initial orientations of ice cluster (red) at $t_0 = 0$, and $t_1 = 100$ ns. First and third row: front view, second and fourth row: bottom view. (b) Schematic illustration describes the viewing direction of the front and bottom view. (c) Regional potential energy ($U_{R.avg}$) of three cases of different ice cluster orientations.

As Fig. 2.7c shows, the initial potential energy ($U_{R.avg}$) of the ice cluster-graphene interfacial region is -1.84 eV when the basal plane faces the graphene surface, and it is lower than the other two cases ($U_{R.avg}$ = -0.31 eV for the primary prism plane and -0.51 eV for the secondary prism plane). During the freezing process, the $U_{R.avg}$ from the first two cases (P1 and P2 plane facing the graphene surface) gradually decreased as the ice cluster rotated to have the basal plane parallel to the surface. Consequently, the $U_{R.avg}$ from three different orientation cases converged to a similar value (~ -2.0 eV at t_1 = 100 ns).

As the lower $U_{R.avg}$ represents the more stable configuration, the configuration where the basal plane and graphene are parallel is the most stable. This explains the alignment of graphene flakes in Fig. 2.6 and the ice cluster rotation of the P1 and P2 cases in Fig. 2.7. Moreover, after the alignment of the ice cluster for the basal plane parallel to graphene, the hexagonal structure of water molecules started forming around the ice cluster, showing ice growth. As discussed above in Fig. 2.5, the ice crystal mainly grows in a direction normal to the P2 or P1 plane, i.e., parallel to the basal plane. Therefore, with graphene-water surface interactions, ice mainly grows in a direction parallel to graphene surface.

2.6 Conclusions

In this research, the fundamental controlling mechanisms of water-ice interface propagation were investigated through molecular dynamics. The maximum propagation speed of the water-ice interface appeared at 252 K. The competition between self-diffusivity and thermodynamic driving force results in an optimal temperature for maximum ice growth speed. Water-ice interfacial energy depends on the orientation of

water-contacting ice surface, and a higher interfacial energy leads to a faster ice propagation speed. Thus, the ice propagation speed depends on water-ice surface orientation. Graphene-water surface interactions align ice clusters or graphene flakes to have a minimum energy state, in which the basal plane of the ice crystal is parallel with the graphene surface. As a result, the orientation of ice crystals and the ice growth speed and direction can be changed by controlling surface interactions. This study provides insights to ice propagation control mechanisms for effective freeze cast structuring and its broader applications.

Chapter 3
Rayleigh-Bénard Convection and Freezing Propagation during Water-Ice Phase Change

3.1 Abstract

The water-ice phase change and convection behaviors with a bottom surface cooling were investigated for the fundamental understanding and control of the ice front propagation. The convection flow profiles, and the geometry and propagation of water-ice interface were examined using the computational fluid dynamics simulations with different temperature and geometrical conditions. This study revealed that the water-ice interface has the largest spatial variation in height when the temperature of maximum density (277K) is applied to the top boundary or the density inversion parameter is the unity, due to the effect of Rayleigh-Bénard convection and propagation of the water-ice interface. The geometrical confinement by the water container, characterized by the aspect ratio, also influences the convection profiles. The Rayleigh-Bénard convection becomes more prominent as the aspect ratio Γ (the height-to-diameter ratio) increases, which enhances the convection heat transfer or the Nusselt number but lowers the ice propagation speed. Since the water-ice interface propagates more unevenly with a faster propagation speed and more developed convection, the largest interface height variation appears at $\Gamma = 0.67$, as a result of the competition the Rayleigh-Bénard convection and the interface propagation on the aspect ratio. As this research identifies the control of the Rayleigh-Bénard convection, ice front propagation and interface shape, the findings will benefit the applications of water-ice phase change, such as freeze casting.

3.2 Disclosure

Chapter 3 is a modification of the developing manuscript: Yu-Kai Weng, Seungha Shin*, Mian Umar Saeed, Mohammad Bahzad, Kenneth D. Kihm, and Douglas S. Aaron, " Rayleigh-Bénard Convection and Freezing Propagation during Water-Ice Phase Change"

The dissertation author listed in this publication directed and supervised the research which forms the basis for this manuscript.

3.3 Introduction

Natural convection, which is generated by thermal buoyancy originating from the temperature dependence of density, plays an important role in various heat transfer applications, such as heat exchangers, solar water heaters [75-77], and passive cooling systems in electronic devices [78], where active cooling with external power source is unavailable or inefficient. In addition, natural convection has been extensively investigated to understand natural phenomena, like atmospheric motion [79, 80] and ocean circulation [81]. Since the convection heat transfer coefficient is determined by temperature (T) profile, understanding of flow patterns that affect the T profile is critical to evaluate the heat transfer efficiency in natural convection [82, 83].

Rayleigh-Bénard (RB) convection is one of representative natural convection patterns, which can be observed in a fluid layer heated by the horizontal boundary at the bottom while cooled at the top boundary [84, 85]. Due to the convenience of experimental setup and clearly-identified physical mechanism [86], RB convection has been used to study various issues, such as the stability [87, 88] and spatial-temporal chaotic behaviors [89], in natural convection. Water is a widely used working fluid in heat transfer systems due to their large heat capacity, availability, etc.; thus, the RB convection of water has been widely studied [90-92].

Water has a unique temperature-density relation in that the density increases with increasing temperature up to the temperature of maximum density, $T_{\rho.max}$ (277 K, or 4℃) and then decreases [93]. This enables a flow circulation with an inverse temperature gradient, where the bottom surface is colder, and the top surface is warmer, can be recognized as Rayleigh-Bénard (RB) convection. In the past three decades, RB convection has been extensively reported by experiments [94, 95] and numerical simulations [96, 97]; however, research on RB convection of water during freezing, with an inverse temperature gradient is rare.

Inverse temperature setting of water is employed in freeze casting, used to fabricate porous materials like polymer [98] and ceramic biomaterials [99]. When a fluid with suspended particles is solidified, the suspended particles are rejected by solidifying fluid and that templates porous structures [28]. Thus, the freeze cast structure has a strong sensitivity on the directionality of the solidification [22], and the understanding and control of ice propagation behaviors [100] is important in the freeze casting using water. As interference of the solidification [101] and melting [102] process by convection has been reported, RB convection by the inverse density profile is also expected to perturb the water-ice interface during freezing. With our interest in the synthesis of directional graphene aerogel using freeze casting, we studied the convection behaviors and ice propagation during water-ice phase change process with inverse temperature gradient. Computational fluid dynamics (CFD) was employed as a primary tool in this work for effective analysis of the fluid flow behaviors and phase changes [103, 104].

The Rayleigh-Bénard convection of water during freezing was investigated under different geometrical and physical conditions in CFD simulations. Specifically, the boundary temperatures which determine the density profile and the container aspect ratio to impose geometrical constraint were varied as main control parameters. In this paper, these control parameters and the simulation details are introduced, followed by the discussion on their effects on the flow profile, water-ice interface shape, freezing propagation, and overall heat transfer performance.

3.4 Methodology

To investigate the Rayleigh-Bénard convection under an inverse temperature gradient and its effect on water-ice phase change, water in a cylindrical container, as depicted in Fig. 3.1, was simulated near the freezing temperature (273 K) using ANSYS-Fluent computational fluid dynamics (CFD) package [105]. The height H and diameter D of the water are 40 mm and 20 mm, respectively, under the benchmark condition. The temperatures of the top and bottom horizontal surfaces were fixed at T_h and T_c during our simulations, and the benchmark simulations employed T_h = 277 K and T_c = 270 K. The sidewalls of cylindrical water were assumed to be adiabatic. The density, viscosity, and thermal expansion coefficient of the water were considered as a function of temperature, while the other thermophysical properties were assumed to be constant. All the properties and their temperature dependence were obtained from the referenced database [106].

In natural convection, the ratio of diffusion and convection, i.e., Rayleigh number Ra, is used as a main control parameter in general [107], which is defined as

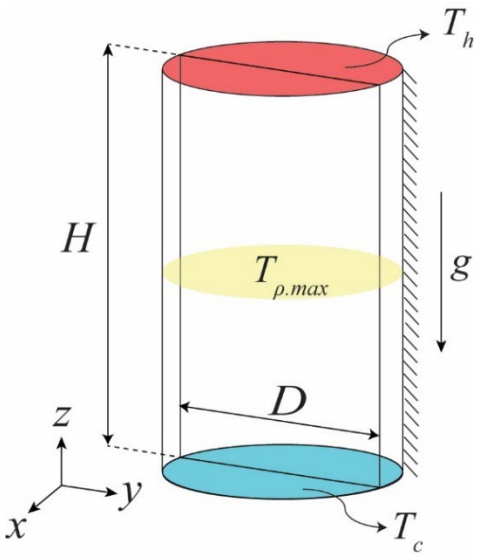

Figure 3.1 Schematic diagram of simulation domain for Rayleigh-Bénard convection.

$$Ra = \frac{\rho g \beta \Delta T L_c^3}{\mu \alpha}, \tag{3.1}$$

where ρ is the density, β is the thermal expansion coefficient, ΔT is the temperature difference, L_c is the characteristic length (height, H in this work), g is the gravitational acceleration, μ is the dynamic viscosity, and α is the thermal diffusivity. In conventional RB convections, where a higher temperature is applied to the bottom surface, *Ra* has been reported to have a strong influence on the structure of convection rolls [108]; into addition to physical properties such as viscosity, *Ra* effects on the RB convection have been extensively investigated [109]. Since the buoyancy caused by temperature gradient is a driving force of RB convection with an inverse temperature gradient, boundary temperatures were varied in this study, which also changed *Ra* due to the variation of the density, viscosity, and thermal expansion coefficient. For effective analysis, fixing the maximum T difference ($\Delta T = T_h - T_c = 7$ K), temperatures of two boundaries, i.e., T_h and T_c, were changed in the simulations. The temperature setup, which can induce a density inversion (the density increases with temperature), was characterized by the density inversion parameter (Θ_m) that is defined as $\Theta_m = (T_{\rho.max} - T_c)/(T_h - T_c)$. Our simulations employed T_c ranging from 267 K to 273 K and T_h ranging from 274 K to 280 K as Table 3.1 shows, and thus, Θ_m and *Ra* ranged from 0.59 to 1.45 and from 1.61×10^5 to 1.83×10^6, respectively for the fixed T_h - T_c of 7 K. For $\Theta_m < 1$ ($T_c > 270$ K), the temperature of the maximum density $T_{\rho.max}$ (277 K) is located between the top and bottom boundaries, and the density does not change monotonically; as the distance from the bottom surface increases, the density first increases and then decreases after the maximum density. On the other hand,

Table 3.1 Density inversion parameters (Θ_m) and Rayleigh numbers (Ra) with different prescribed boundary temperatures

T_h (K)	T_c (K)	Θ_m	Ra ($\times 10^5$)
280	273	0.59	1.61
279	272	0.74	4.73
277	270	1.00	10.6
275	268	1.31	15.9
274	267	1.45	18.3

$\Theta_m > 1$ ($T_c < 270$ K) leads to an inverse water density gradient over the whole simulation region.

In addition to the boundary temperatures, the influence of geometrical constraint on the RB convection has been reported to be significant in several studies. Experimental [110] and numerical studies [111] show that the aspect ratio of the container alters the convection patterns, including the number of RB convection rolls [107]. The RB convection under an inverse temperature setup is also expected to be affected by the geometry, which is characterized by the aspect ratio (Γ), i.e., the ratio of the horizontal to vertical dimensions of the system domain ($\Gamma = D/H$). To adjust the aspect ratio (Γ), the diameter, D was varied from 20 to 80 mm ($0.5 \leq \Gamma \leq 2$), while H was maintained at 40 mm, as in Table 3.2. As H was used as a characteristic length, Ra does not change with the variation of Γ only.

In the reference to the coordinate system shown in Fig. 3.1, the governing equations based on the continuity, momentum and energy conservations are described as:

$$\frac{\partial \rho}{\partial t} + \frac{\partial}{\partial x_i}(\rho u_i) = 0, \tag{3.2}$$

$$\frac{\partial \rho u_i}{\partial t} + \frac{\partial}{\partial x_j}\left(\rho u_i u_j\right) = -\frac{\partial p}{\partial x_i} + \frac{\partial \tau_{ij}}{\partial x_j}, \quad \text{and} \tag{3.3}$$

$$\frac{\partial \rho e}{\partial t} + \frac{\partial}{\partial x_j}\left[\mu_i \rho (e + \frac{\sum u_i^2}{2})\right] = \frac{\partial}{\partial x_j}\left[p u_j + \tau_{ik} u_k\right], \tag{3.4}$$

where ρ is the density, e represents the specific internal energy, p is the pressure, and μ is the dynamic viscosity. The subscript i, j, and k are the indices for direction in the Cartesian coordinate system in Fig. 3.1. The viscous stress τ_{ij} is given by:

Table 3.2 Dimensions of the simulated water container and the aspect ratio (Γ)

D (mm)	H (mm)	Γ
20.0	40	0.50
26.6	40	0.66
40.0	40	1.00
80.0	40	2.00

$$\tau_{ij} = (\mu + \mu_t)\left[\left(\frac{\partial u_i}{\partial x_j} + \frac{\partial u_j}{\partial x_i}\right) - \frac{2}{3}\delta_{ij}\frac{\partial u_k}{\partial x_k}\right], \quad (3.5)$$

where δ_{ij} is the Kronecker delta function, μ is the dynamic viscosity, and μ_t is the dynamic eddy viscosity, which is estimated by the k-ε turbulent model [112].

The SIMPLE [113] pressure-velocity coupling algorithm was introduced to solve the governing equations. The standard scheme is used to discretize pressure, while the second-order upwind methods are used to discretize the momentum and energy transport. The turbulent kinetic energy and turbulent dissipation rate were discretized by the first-order upwind method, and the first-order implicit scheme was also applied to discretize the time. The time step of the simulations was set in the range from 10^{-1} to 10^{-3} s, and the total simulation time was 1200 s. The convergence of the solution was assumed when the maximum relative error achieves 10^{-4}.

During the RB convection, the circulating flow creates the inhomogeneous velocity and temperature profile, which locally enhance or suppress the water-ice interface propagation. Consequently, the shape and location of the water-ice interface changes. To characterize the effect of the RB convection during the freezing process, the freezing propagation speed (u_f) was calculated using the average distance of water-ice interface from the bottom of the container ($z_{w/i,avg}$) with respect to time (t). Also, the spatial variation of the water-ice interface that represents the interface shape was characterized by the standard deviation of the interface height (σ_z), as:

$$\sigma_z = \sqrt{\frac{\sum_{j=1}^{N}(z_{w/i,j} - z_{w/i,avg})^2}{N}}, \quad (3.6)$$

where $z_{w/i,j}$ is the interface height from the bottom at the j-th data point, and N is the total number of the data point at the water-ice interface.

To characterize the convection heat transfer, Nusselt number Nu, which is defined as the ratio of the convective and conductive heat transfer, is calculated using [114]:

$$Nu = \frac{hL_c}{k}, \tag{3.7}$$

where h is the convection heat transfer coefficient, L_c is characteristic length (H in this research), and k is the fluid thermal conductivity. In this work, the heat transfer coefficient is obtained by calculating the ratio of the heat flux through the container to the temperature difference ($h = q''/\Delta T$), and the heat flux q'' is extracted from the simulation data.

3.5 Results and Discussion

The interaction between the Rayleigh-Bénard convection and the freezing makes the water-ice interface nonuniformly propagates from the bottom, while the convection flow carries the energy and momentum toward the interface. This non-uniform interface due to the Rayleigh-Bénard convection in the density inversion temperature ranges agrees with the prior experimental observations [115, 116]. Eventually, the interface developed into a concave shape, where the interface near the sidewall has a higher propagation distance than that at the center, as shown in Fig. 3.2. After 1200 sec, temperature and velocity profiles do not change much, and thus, the RB convection and water-ice interface properties at 1200 sec were analyzed under various freezing conditions.

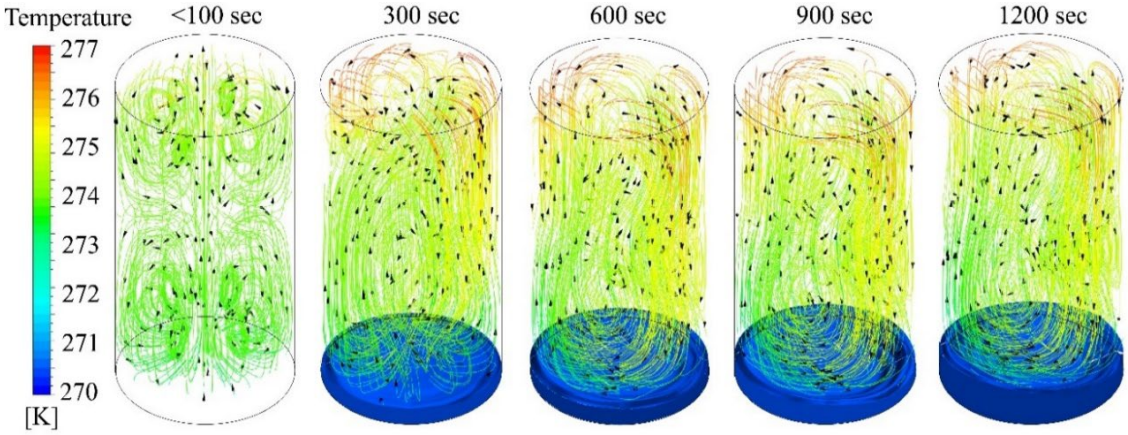

Figure 3.2 The propagation of water-ice interface through the freezing times. The color contour in the streamline represents the water temperature, the blue surface near the bottom represents the water-ice interface (the surface of ice propagates from the bottom), and the arrows in the figures represent the velocity vectors.

The velocity and temperature distributions of water undergoing the RB convections were first examined with different density inversion parameters (Θ_m). Figures 3.3(a)-3.3(e) demonstrate the temperature distribution (in color) and velocity vectors (with arrows) in the vertical cross-section of water for Θ_m = 0.57, 0.71, 1.00, 1.28, and 1.45. When Θ_m is less than unity (i.e., $T_c < T_{\rho.max} < T_h$), the convection flow develops a primary circulation roll at the bottom corner, and several secondary rolls co-exist at the other corners. In contrast, for $\Theta_m > 1$, a single dominant circulation that occupies the entire container was observed. This phenomenon is attributed to the monotonic density change as T_h is lower than $T_{\rho.max}$.

The different RB convection behaviors by different Θ_m affect heat transfer efficiency between the top and bottom surfaces and the freezing process. To examine the effect of Θ_m on the heat transfer and water-ice phase change, we calculated the Nusselt number (Nu) and the water-ice interface propagation speed (u_f). As Fig. 3.4 shows, Nu decreases with increasing Θ_m while the freezing propagation speed increases. The relationship between Nu and Θ_m matches with the numerical estimation from other researchers [117]. The reduced heat transfer at greater Θ_m's even with a constant temperature difference (ΔT = 7 K) is attributed to slower convection with a simple structure due to greater water viscosity at lower temperature and monotonic density profiles at larger Θ_m's. In contrast, a lower Nu in the liquid water region at greater Θ_m's demonstrates lower heat flux to the water-ice interface region, which promotes the water-ice phase change. Moreover, a lower T_c at larger Θ_m increases the thermodynamic driving force for the water freezing [100] and enhances the water-ice interface propagation u_f.

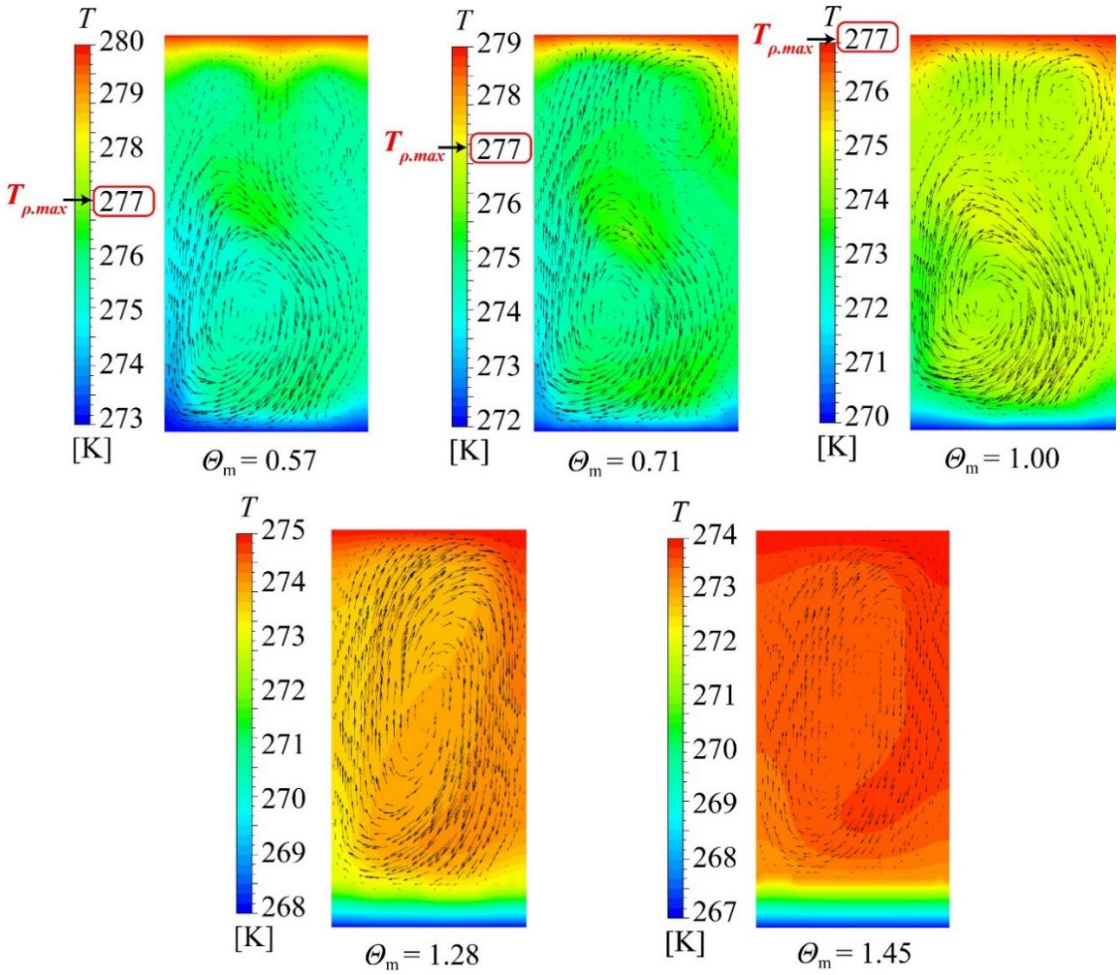

Figure 3.3 The instantaneous snapshot of temperature and velocity profile in the vertical cross-section of the container under different inversion parameters at 1200 seconds freezing times, Θ_m = 0.57, 0.71, 1.00, 1.28, and 1.45. The water temperature is represented by color following the scale in the left, and the arrows show the velocity vectors.

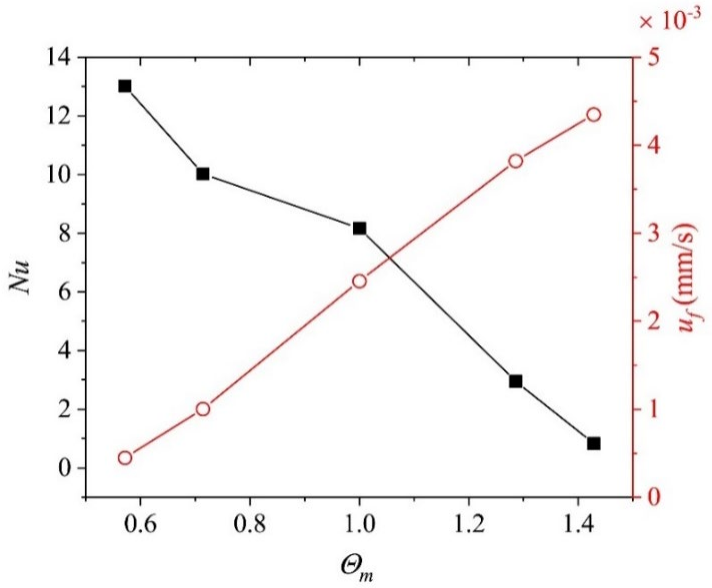

F

Figure 3.4 Nusselt number (*Nu*, black filled squares) for the heat transfer between the top and bottom boundaries and the freezing propagation speed (u_f, red empty circles) with respect to the density inversion parameter (Θ_m).

Consequently, the competition between the interface propagation and the convection effect leads to the variation of the interface height in different Θ_m cases, as shown in Fig. 3.5a. The standard deviation of the interface height (σ_z), characterizing the height variation, was calculated by analyzing the spatial distribution of the water-ice interface as Fig. 3.5b. The largest variation (σ_z) of the interface height appears in the case of Θ_m equal to unity; that is, the shape of the water-ice interface at $\Theta_m = 1$ has a more curved (bowl-like) shape while a more flattened water-ice interface appears a Θ_m deviated from unity. More significant convection flow or faster ice formation contributes to flattening the water-ice interface, and the opposite trends of the convection and ice propagation with Θ_m lead to the maximum variation at $\Theta_m = 1$.

In addition to the density inversion parameter (Θ_m), the aspect ratio of the container ($\Gamma = D/H$) affects RB convection because the geometry confinement restricts the development of convection circulation rolls. Figure 3.6 presents the temperature and velocity distributions of the RB convection under different aspect ratios. In the container with $\Gamma = 2$, two convection rolls, which symmetrically occupy the fluid domain, were observed in the cross-section, while a single dominant circulation roll appears when Γ is equal to or lower than unity. These observations agree that the size of the fully developed Bénard convection cell λ is close to twice the characteristic length (i.e., height $\lambda = 2H$) in the rigid top and bottom boundary conditions without a geometrical constraint on the side [118]. When the longest horizontal length of the container (D) is less than the unconstraint Bénard cell size λ but larger than H ($H \leq D < 2H$ or λ), two convection rolls appear; however, one of them occupies a majority part of the container, which creates an asymmetric flow field.

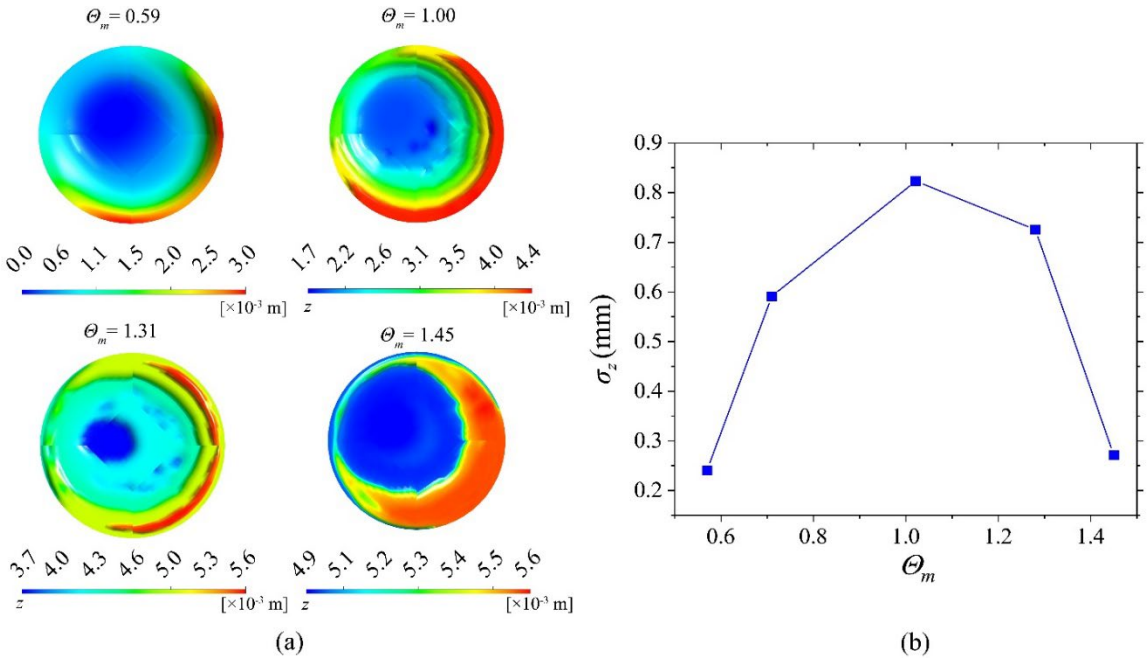

Figure 3.5 (a) The distribution of the water-ice interface height from the top view and (b) the standard deviation of interface height (σ_z) with respect to the density inversion parameter (Θ_m).

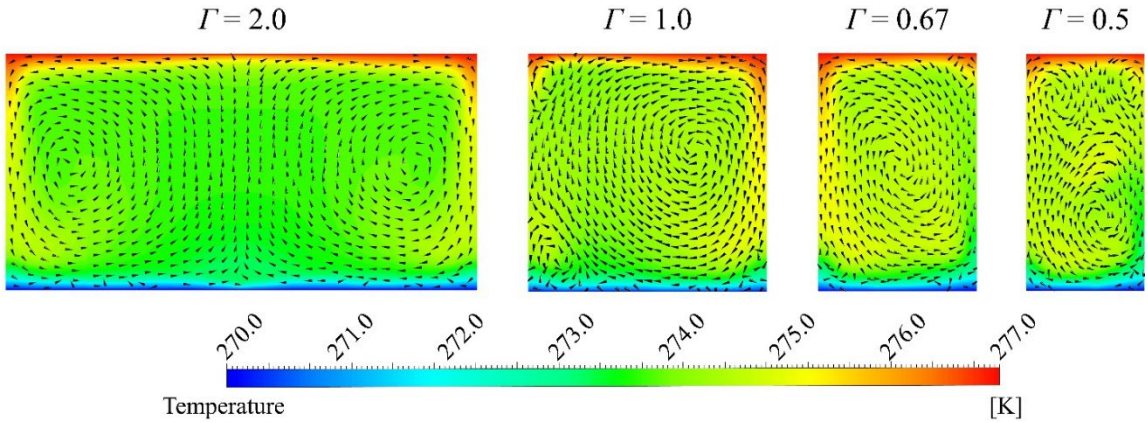

Figure 3.6 Temperature and velocity profile in the vertical cross-section of the container under different aspect ratios, i.e., Γ = 2.0, 1.0, 0.67, and 0.5. The water temperature is represented by color following the scale below, and the arrows show the velocity vectors.

The transition from a symmetric to asymmetric state can be recognized as spontaneous symmetry-breaking [119]. When the horizontal length is further reduced to less than the height of the container ($D < H$), the development of a single convection roll is also restricted as the diameter of a single convection roll (d_c) ranges from 1 to 1.4 times the container height ($d_c = \lambda/2 \sim H$) in RB convection [120]. Consequently, RB convection is suppressed by reducing the aspect ratio (Γ).

The effects of the aspect ratio (Γ) on the heat transfer (Nu) and the water-ice interface propagation (u_f) were examined with the different inversion parameters (Θ_m = 0.75, 1.0, and 1.25), as shown in Figs. 3.7a and 3.7b. Nu increases with increasing Γ (increasing D) for all three Θ_m's due to a less restricted RB convection with larger Γ or D, enhancing the heat transfer. Above Γ of one, as convection circulation rolls can be fully developed without geometrical constraints, Nu does not change significantly, which agrees with a previous computational study [111]. The sensitivity of Nu to Γ also decreases with increasing Θ_m as the heat supply is reduced at larger Θ_m. The propagation speed of the water-ice interfaces (u_f) also shows the opposite dependence on Γ, i.e., u_f decreases with increasing Γ because the freezing process slows down by increasing convective heat transfer. With a given Θ_m, temperature boundary conditions are identical, and thus, the reduction in u_f at larger Γ's can be attributed solely to the enhanced convection heat transfer to the water-ice interface, which suppresses the freezing process. Here, Nu obtained from the simulation in this study is in a good agreement with the results from experiments [121] and CFD [107] simulations in prior RB convection studies, which

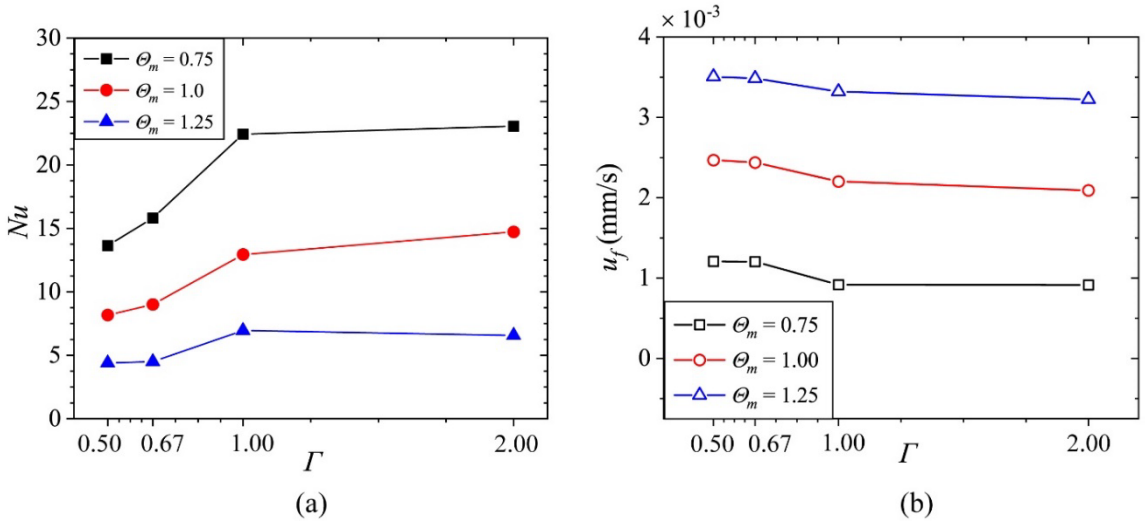

Figure 3.7 (a) Nusselt number (Nu) for the heat transfer between the top and bottom boundaries and (b) the freezing propagation speed (u_f,) with respect to the aspect ratio ($\Gamma = D/H$) at three different density inversion parameters (Θ_m = 0.75, 1.0, and 1.25).

were conducted under similar conditions ($Ra \sim 10^6$) but via heating (not inverse temperature gradient), as in Table 3.3. This agreement suggests that the dependence of heat transfer efficiency in RB convection on Ra is similar in both heating and cooling conditions and validates our simulation results.

RB convection alters the circulation flow patterns and interface propagation during freezing. As a result, the shape of the water-ice interface changes with Γ as presented in Fig. 3.8a. The figure shows that the lower surface region (blue and cyan) of the interface deviates from the center, and the higher surface region (red) is only distributed on the single side of the interface in the two low aspect ratio cases (Γ = 0.5 and 0.67). These asymmetric interface patterns indicate that the entire interfaces are affected by a single direction of a convection flow, as shown in Fig. 3.6. On the contrary, interface propagation for the largest aspect ratio case (Γ = 2.0) shows a more consistent and symmetric propagation, which matches the temperature and velocity profile shown in Fig. 3.6. The analysis of these figures shows that geometrical confinement restricts the development of RB convection, which affects the convection flow path inside the container and the resulting overall heat transfer and water-ice interface propagation and shape.

Figure 3.8b shows that the interface shape has stronger sensitivity on the aspect ratio (Γ) when the density inversion parameter is unity (Θ_m = 1), which has the largest variation of interface height in every aspect ratio. As the geometrical confinement is reduced with an increasing aspect ratio (Γ), the convection circulation rolls can develop more completely,

Table 3.3 Comparison of *Nu* from this study with prior research

Source	Method	Container	Γ	Ra ($\times 10^6$)	Nu
Ref. [121]	Exp.	Cubical	1.0	1.0	**7.883**
Ref. [107]	CFD	Cylindrical	0.5	1.0	**8.02**
Current work ($\Theta_m = 1$)	CFD	Cylindrical	0.5	1.06	**8.81**

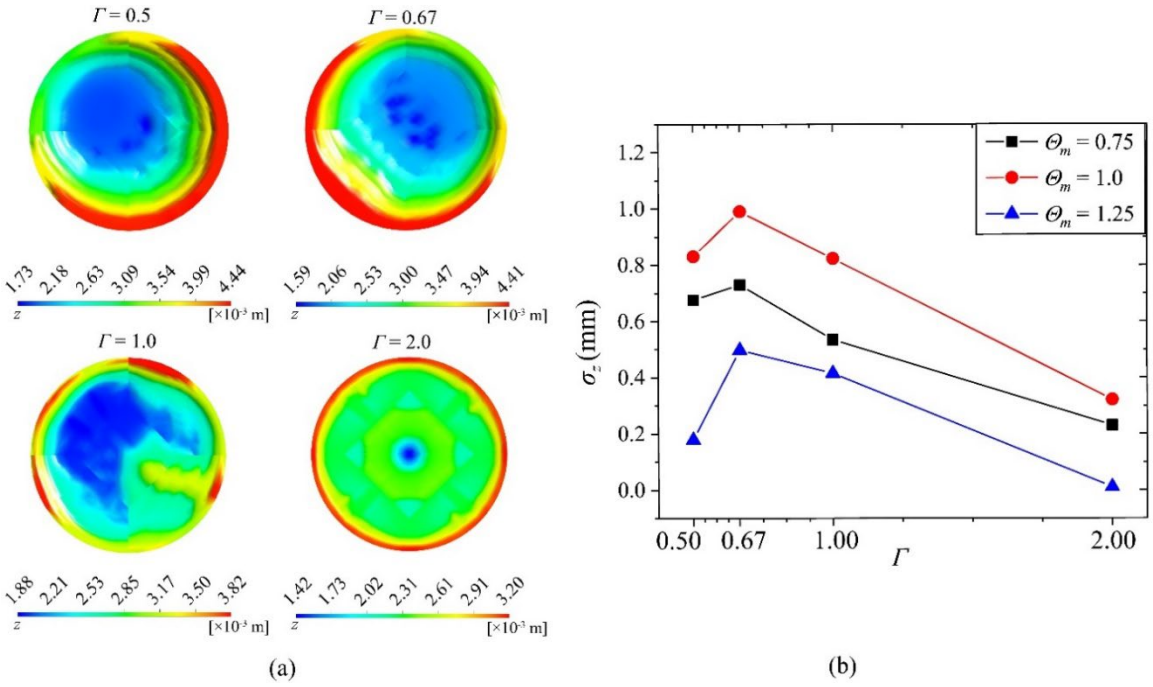

Figure 3.8 (a) The distribution of the water-ice interface height from the top view and (b) the standard deviation of interface height (σ_z) with respect to the aspect ratio ($\Gamma = D/H$).

which makes the convection effect increases with Γ when $\Gamma < 1$ and start to converge when $\Gamma > 1$. Both more significant RB convection and faster interface propagation contribute to the height variation of the water-ice interface, but they have the opposite trends with respect to Γ. Thus, the variation σ_z is maximized at 0.67 in Γ in all three Θ_m cases.

3.6 Conclusions

The water-ice interface propagation and the Rayleigh-Bénard convection during freezing were investigated using computational fluid dynamics with inverse temperature and density profiles. Our simulations show that the convection structure becomes simpler and slower as the density inversion parameter increases because the stronger phase changing tendency at lower temperatures interrupts the convection heat transfer. Hence, the heat transfer efficiency decreases with an increasing density inversion parameter; conversely, the speed of water-ice interface propagation has the opposite dependency on inversion parameter because the increasing convective heat transfer suppresses the freezing process. Consequently, the competition between the effects of Rayleigh-Bénard convection and the water-ice interface propagation makes the maximum variation of the interface appear at the inversion parameter equal to the unity. The geometrical confinement of the container, which is characterized by aspect ratio Γ, restricts the development of RB convection rolls, which decreases the heat transfer or Nu. Nu increases with increasing aspect ratio below the unity ($\Gamma < 1$), but the increase above one is insignificant. In contrast, the interface propagation speed is reduced with an increasing aspect ratio due to enhanced heat transfer. Finally, the opposite trends between the RB convection and the water-ice interface propagation speed with aspect ratio led to the largest variance of the water-ice interface at

Γ, equal to 0.67. Our findings demonstrate that ice propagation speed and water-ice interface shape can be effectively controlled by the temperature setup and geometrical confinement. Therefore, this report will benefit the applications of water-ice phase change, such as freeze casting.

Chapter 4
Surface Interaction Effect on Ion Transport with Convective Flow in Graphene Nanochannel

4.1 Abstract

The influence of hydrodynamic, thermodynamic, and geometric conditions on ion transport was investigated with consideration of ion-water surface interaction for understanding and effective control of ionic mobility. The drift velocity and ion-graphene distance distribution were examined by analyzing the atomic trajectory from molecular dynamics. The ionic mobility is affected by the ion-graphene surface interaction, which leads to the highest mobility appearing at the lowest interaction strength. The channel size changes the probability of the ions being affected by surface interaction. Thus, a larger channel size not only increases mobility but also reduces the sensitivity of the mobility to the interaction strength. The surface interaction is a function of temperature, and the higher interaction strength attracts more ions into the effective range of the surface interaction. Therefore, stronger interaction strength leads to a higher sensitivity of ionic mobility to temperature.

The convective flux alters ionic mobility due to the coupling effect. The larger channel size enhances the coupling effect on ionic mobility because fewer ions can be affected by surface interaction. On the other hand, the higher temperature raises the kinetic of the atoms in the whole system. Consequently, the sensitivity of ionic mobility to the coupling effect is reduced. The findings from this work can provide insights into the ion transport controlling mechanisms for the performance of electrode enhancements.

Keywords: Ion transport, Surface interaction, Molecular dynamics

4.2 Disclosure

Chapter 4 is a modification of a manuscript preparing for publication: **Yu-Kai Weng**, Seungha Shin*, Kenneth D. Kihm, Mohammad Bahzad, and Douglas S. Aaron, "Surface Interaction Effect on Ion Transport with Convective Flow in Graphene Nanochannel". The dissertation author listed in this publication directed and supervised the research which forms the basis for this publication.

4.3 Introduction

Ion transport through nanofluidic devices has been an attractive research topic over past a few decades due to their significance in understanding of various mass transport phenomena such as high gas selectivity [122] and fast ion sieving [123]. The large surface-to-volume ratio in nanostructure increases the influence of surface-fluid interaction, which can enhance the performance of water desalination [124] and ion/molecules separation [125]. Also, the high surface-to-volume ratio makes the material choice of the nanofluidic system more important. Due to the high surface area and the outstanding thermal and electrical conductivity, graphene has been selected as a material for nanofluidic devices. Here, we study ion transport in graphene nanochannels with an interest in the charge transport within graphene electrodes of redox flow batteries (RFB). Ions in RFB are transported by not only electrical field but also the convective flow driven by the pressure gradient [126]. Thus, the study on the convective ion transport through graphene nanochannels will benefit the understanding of the surface interaction effect from the channel wall [127-129]. The surface treatments of the graphene, such as doping and

functionalization enable to modify the thermal conductivity [23], wettability [130], and electrical conductivity [131]. Moreover, the surface interaction between carbon and water molecular changes the crystal surface of the ice during the freezing process [100].

The geometrical confinement of the channel has an important contribution on the ion transport. First, the alignment of the channel and the distance between two surfaces affect the bulk velocity of the ion solution. Second, the size of the channel also affects the probability of the interaction between the ion and channel surfaces. The study reports that the ion current rectification occurs when switching the polarity of the potential across the cone-shape nanopore. Thus, ion transport has a strong dependency on the channel size [132]. In addition to the channel size effect, the temperature represents the kinetic distribution of the atoms in the system. Thus, different system temperatures change the mobility of ions and waters. Moreover, several physical properties that change the ion transfer behavior, such as solvent kinematic viscosity, solute diffusivity, and the surface interaction between the ion and graphene are also a function of the system temperatures. The higher feed temperature decreases the ion rejection ratio of the nanofiltration membranes are also reported [133]. Therefore, the temperature effect has a significant contribution to the efficiency of ion transport [134]. To improve the performance of the redox flow battery, the ion transport through the graphene nanochannel has been studied by several researchers in the experiment [135] or numerical simulation [136, 137]. Although ion transport through the carbon nanostructures has been reported in various conditions, such as types of the structure [138, 139] and solute concentration [140], the detailed knowledge of the intermolecular interaction effect on the ion transport still needs

to be identified. To achieve the objective that increase the ion conductivity of graphene electrodes, the ion transport properties under various channel sizes, temperatures, and surface interaction strengths are studied.

In this research, the ion transport through the graphene nanochannel was investigated by molecular dynamics (MD) simulations to have comprehensive knowledge of the surface interaction effect on the ion transport. We have controlled magnitudes of the interaction strengths as well as pressure gradient for convective flow channel sizes, and system temperatures. For diverse cases of channel conditions, we measured the drift velocity with respect to electrical field or pressure gradient and characterized the ionic mobility and convective ion transport. Based on the results from the simulations and analysis, the surface interaction effects on ion transport with a convective flux were discussed in detail.

4.4 Methodology

All the simulation were conducted using LAMMPS open-source package [141]. The system configuration is shown in Fig. 4.1. The nanochannel is built by two parallel graphene sheets where the width (W) and length (L) are 20 Å and 160 Å, respectively. In the ion transport simulation, the channel width in this work is sufficient to prevent the boundary effect. Also, channel length is long enough to record the trajectory of the ion and suppress the entrance effect. The distance between two graphene sheets (d) is subject to be changed as a control parameter. The channel is filled with water molecules with one potassium ion. The initial location of the ion is 10 Å inside the left boundary and in the center (d/2) of the channel.

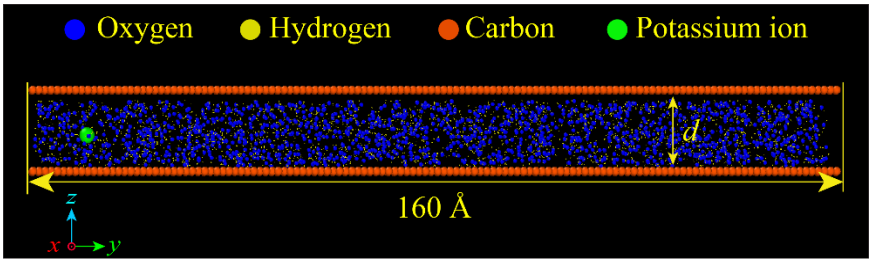

Figure 4.1 System configuration of the graphene channel.

In this ion transport MD simulation, the TIP4P water model [45] is used to obtain the position and force of the water molecules. This rigid water model fixes bond length (O-H) of 9.572 Å with 104.52˚ fixed bond angle (H-O-H), and the charges of O and H atoms are -1.179 and 0.589 elementary charges (e_c), respectively. The massless charge site M is set 0.1577 Å away from the O atom. The rigidity of the water molecules are secured by using the SHAKE algorithm [46]. The long-range Coulombic interactions among the water molecules are calculated by applying the particle-particle particle-mesh (PPPM) algorithm [47].

The carbon-carbon (C-C) interaction inside the graphene was estimated by the Tersoff potential [50]. Newton's equations of motion were integrated by the velocity-Verlet algorithm [51]. In addition, the intramolecular interaction (ϕ_{ij}) between the oxygen, carbon, and potassium ion with a distance less than the cut-off distance (r_c) are calculated by 12-6 Lennard-Jones (LJ) model [48]:

$$\phi_{ij}(r_{ij}) = 4\varepsilon_{ij}\left[\left(\frac{\sigma_{ij}}{r_{ij}}\right)^{12} - \left(\frac{\sigma_{ij}}{r_{ij}}\right)^{6}\right], r_{ij} \le r_c \tag{4.1}$$

where i and j represents atom type, ε_{ij} is interaction energy strength σ_{ij} is the distance at which the potential is zero, r is the interatomic distance, and r_c is the cut-off distance. Moreover, to characterize range of surface interaction, the effective distance (r_{eff}) is defined as 1.75 times σ_{ij}. The effective distance represents the ranges that the ion is affected by surface interaction as Fig. 4.2 shows.

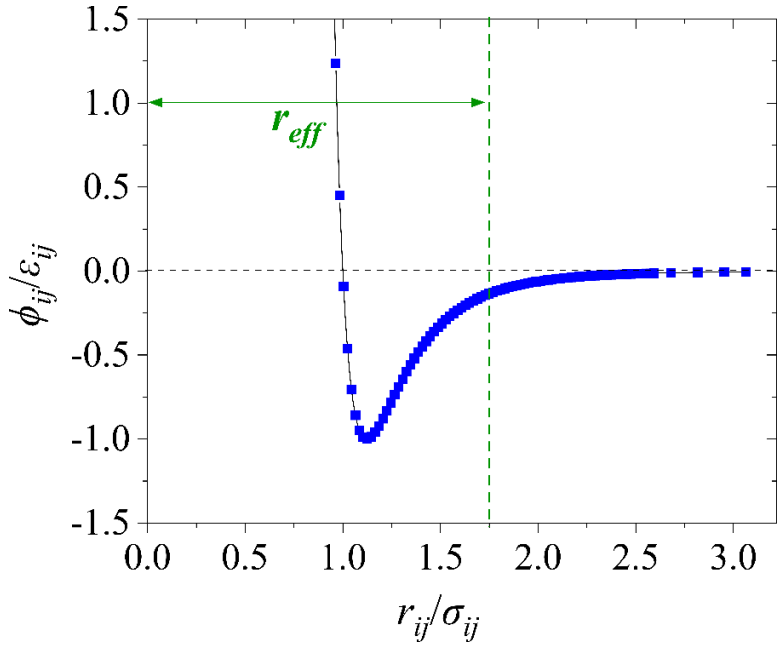

Figure 4.2 Surface interaction energy and effective distance.

In the channel size dependency study, two different sizes of the graphene channel (d = 14 Å and 40 Å) are introduced to create the water and graphene channel system, where the system temperature (T_{sys}) was set at 300 K by Nose-Hoover thermostats. The system initially equilibrated at T_{sys} with an *NPT* ensemble (i.e., fixed number of molecules, pressure, and temperature) for 0.01 nanosecond. After the relaxation, the system was switched to *NVT* (constant number of molecules, volume, and temperature) at T_{sys} for at least 1.0 nanosecond. At this stage, the pressure difference (ΔP) and electric field (E_e) are applied to the system. The trajectory of the Potassium ion is recorded for further analysis of the distance between the ion and graphene wall during the drifting. For the temperature dependency study, two different T_{sys} were set at 300 and 320 K, and the channel size was fixed at 14 Å. Thereafter, the MD simulation procedure of the temperature dependency cases is the same as the size dependency cases.

To characterize the interaction effect on the ion transport, the ionic mobility is calculated through

$$\mu_e = \frac{\Delta u_d \big|_{\Delta p=0}}{\Delta E_e}, \tag{4.2}$$

where μ_e represent the ionic mobility when the electric field is the sole driven force of the ion drifting, the Δu_d is drifting velocity difference of ion in y-axis direction, and ΔE_e is strength difference of the electric fields.

To characterize the surface interaction between the ion and graphene wall, the interaction strength parameter R is defined as:

$$R = \frac{\varepsilon_{ion-carbon,MD}}{\varepsilon_{ion-carbon,ori.}}, \tag{4.3}$$

where $\varepsilon_{ion\text{-}carbon,\ ori}$ is the default interaction energy value between the ion and carbon from the Lennard-Jones model, and $\varepsilon_{ion\text{-}carbon,MD}$, represents the value which is manually controlled during the MD simulation. Larger R indicates stronger surface interaction between the ion and graphene wall. In this work, the interaction strength (R) is set in 0, 1, and 2.

The probability density function $p(z^*)$ is used to examine the relative distance between the ion and the surface of the graphene channel:

$$z^*=z/d, \quad z=\min(z_1,z_2), \tag{4.4}$$

where z^* is nondimensionalized parameter which represents the distance between the ion and the surface (z) normalized by height of the channel (d), z_1 and z_2 are distances of ion from top and bottom channel surfaces, respectively.

4.5 Result and Discussion

When the ion transport is solely driven by an electric field, the drift velocity linearly increases with the increasing electric field. This behavior is expected since ohm's law describes the linear relationship between the current and the electric potential. However, when the electric field becomes significantly large, the ohm's law is invalid due to the electric breakdown and non-linear ion transport behavior occurring in the system. On the other hand, when the pressure difference is the only driven force of the ion transport, the laminar flow field is expected in the low-pressure difference regime. In this work, ionic mobility is studied within the range that drifting velocity has a linear relationship with

electric field and pressure difference to ensure the simulation result and conclusion can be applied to the system on a larger scale.

The relationship between the drifting velocity of ion and two driving forces (electric field and pressure difference) is examined in Fig. 4.3 depicted. Figure 4.3a indicates that the linear growth of u_d is observed when E_e is lower than 100 mV/nm, and the u_d starts to deviate from the linear relationship when E_e is larger than 200 mV/nm. The ion transport driven by pressure difference has a similar behavior, as shown in Fig. 4.3b. The u_d increases linearly with ΔP until 100 bars of pressure difference is reached. Figure 4.3 also depicts that a larger channel size (d) leads to the higher u_d in all E_e and ΔP ranges. For the result validation, the ionic mobility (μ_e) is calculated from the data on the linear region of Fig. 4.3a, which is close to the experimental measurement [142] on the infinite dilution conditions. On the other hand, the sensitivity of drift velocity to the pressure difference from the data on the linear region of Fig 4.3b is slightly higher than the referenced work [143]. The geometrical confinement effect can be the possible reason for the difference since the channel size of the reference work is smaller than the current system.

Once the linear relationship is observed between the drift velocity from two driving forces (E_e and ΔP), the ionic mobility with and without the convective flux can be obtained. Figure 4.4 represents the increment of the drift velocity with an electric field with and without the involvement of the convective flux. The ionic mobility under various conditions can be obtained by measuring the slope of each dataset.

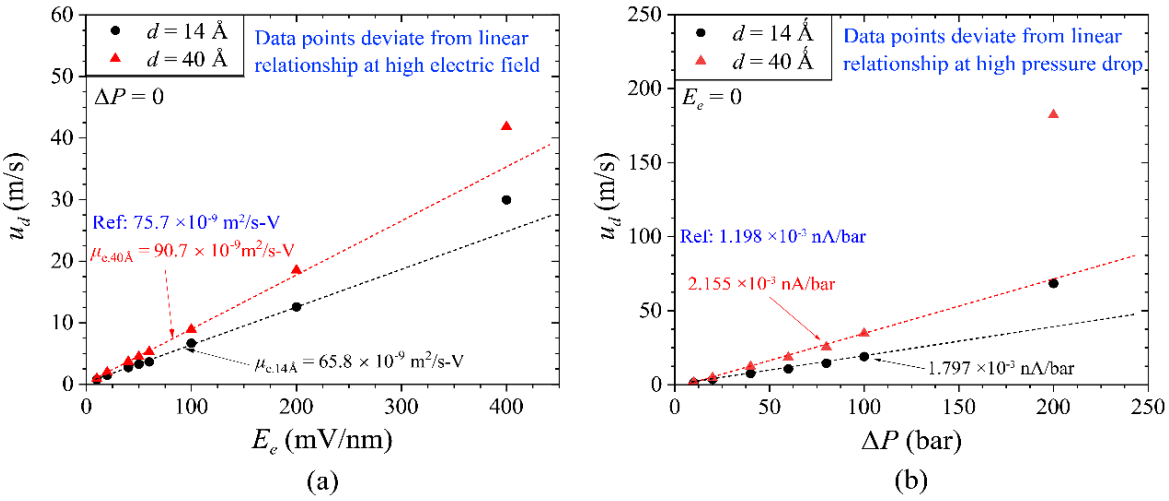

Figure 4.3 The drifting velocity of ion solely driven by (a) electric field, (b) pressure difference.

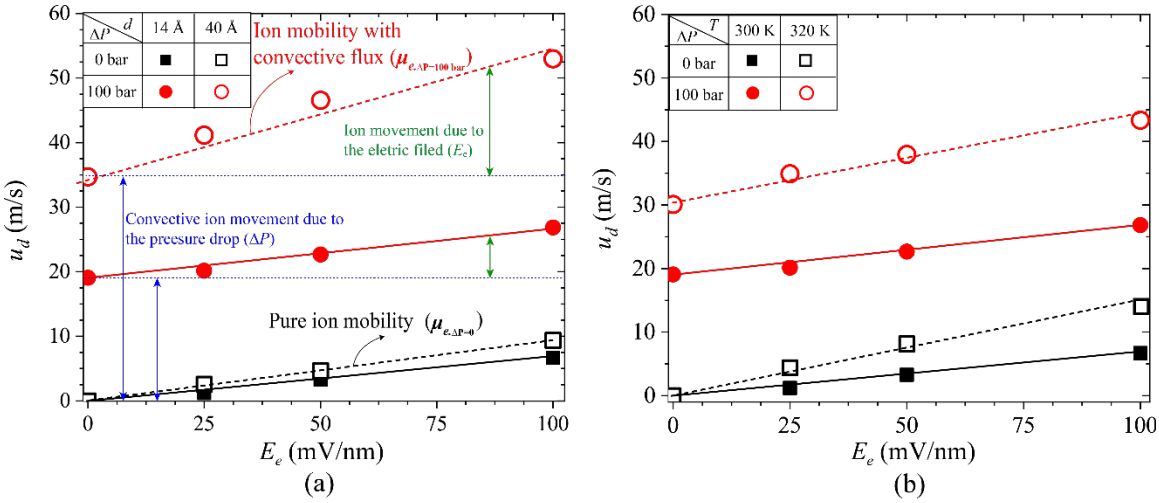

Figure 4.4 The drifting velocity with and without the coupling effect from convective flux under different (a) channel size, (b) temperature.

The figure shows that the ionic mobility with the coupling effect from convective flux (ΔP = 100 bar) is higher than the one without the coupling effect of the convective flux (ΔP = 0). Figure 4.4a indicates that the larger channel size leads to the larger sensitivity of ionic mobility on the pressure difference. On the other hand, Fig. 4.4b shows the ionic mobility increase in higher temperatures. However, the coupling effect is not significant in the same temperature conditions.

When the ion drifts through the graphene nanochannel, the surface interaction between the ion and graphene wall can affect mobility. Figure 4.5a depicts the ionic mobility under different surface interaction strengths and channel size conditions. The figure shows that ionic mobility reaches the maximum value when surface interaction is removed (R = 0). When the interaction strength is increased, the ionic mobility is reduced accordingly. Moreover, a larger channel size leads to greater ionic mobility. The ionic mobility is also affected by convective flux regardless of the channel size, as shown in Fig. 4.5b. However, when the ion transport is coupled with the convective flux, the sensitivity of ionic mobility on channel size is amplified.

In addition to the channel size effect, the temperature can contribute to the ionic mobility changing with different interaction strengths. Figure 4.6a indicates that a higher temperature leads to higher ionic mobility. It is also observed that larger interaction strength makes the sensitivity of the mobility to temperature increase. When the coupling effect from convective flux is involved, the ionic mobility is also changed, as shown in Fig 4.6b.

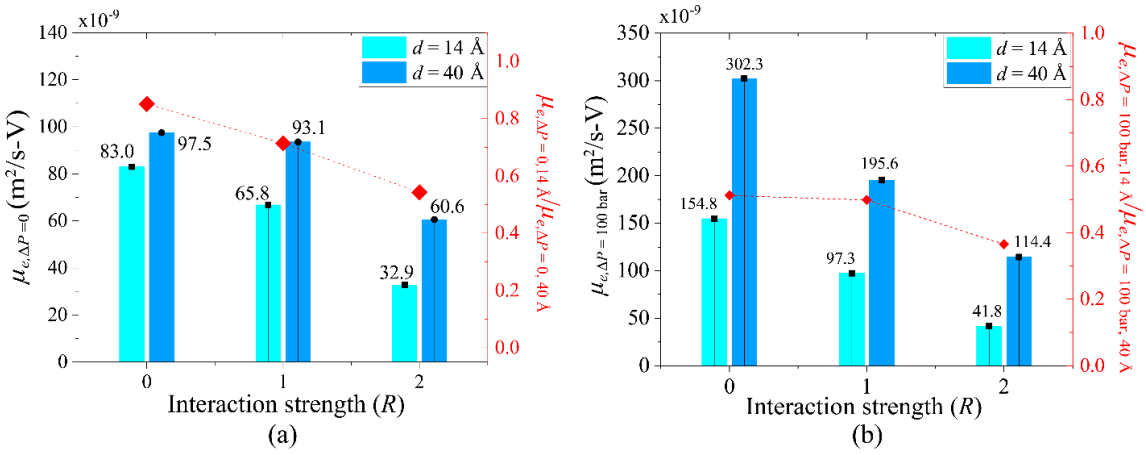

Figure 4.5 The mobility changing from different interaction strength (R) and channel size. (a) Ion transport solely driven by electric field, (b) ion transport is driven by electric field coupled with convective flux (ΔP = 100 bar). Red filled mark and dash line represents the reduction ratio of the ionic mobility.

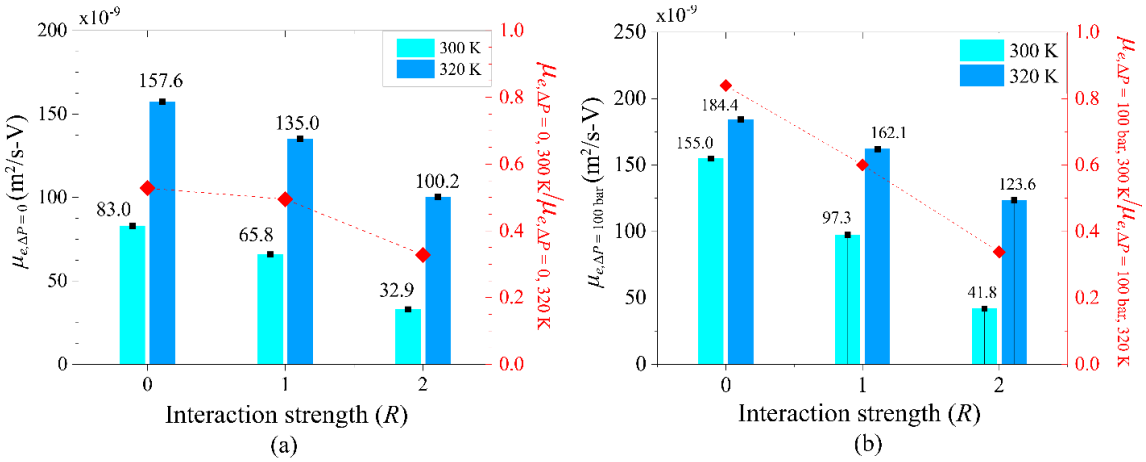

Figure 4.6 The mobility changing from different interaction strength (R) and temperature. (a) Ion transport solely driven by electric field, (b) ion transport is driven by electric field coupled with convective flux (ΔP = 100 bar). Red filled mark and dash line represents the reduction ratio of the ionic mobility.

From the figure, it can be seen that the larger interaction strength still leads to the highest sensitivity of the mobility on the temperature, while the contribution of the temperature effect is less significant in the low interaction strength ($R = 0$) case.

Temperature and channel size differences do not just directly change ionic mobility. The coupling effect from convective flux to mobility is also affected by temperature and channel size difference, as Fig. 4.7 shows. From Fig. 4.7a, it can be seen that the lowest interaction strength leads to the highest mobility increment from the coupling effect. When the channel size increases from 14 Å to 40 Å, by coupling effect from convective flux can be observed in Fig. 4.7b. The figure indicates that a larger channel size not only leads to larger ionic mobility but also increases the coupling effect in all interaction strength conditions. Moreover, the strongest coupling effect at larger channel size conditions appears at the lowest interaction strength. On the other hand, the coupling effect on ionic mobility significantly decreases at a larger temperature, as shown in Fig. 4.7c. The figure also depicts that the mobility difference between interaction strength reduces in higher temperature conditions.

The physical mechanisms of ionic mobility changing from the interaction strength and coupling effect are investigated by examining the distance distribution function as shown in Fig. 4.8. From Fig. 4.8a, the ion have a higher tendency to distribute near the center of the channel ($z^* > 0.3$) with less resistance from the surface interaction when R equals 0.

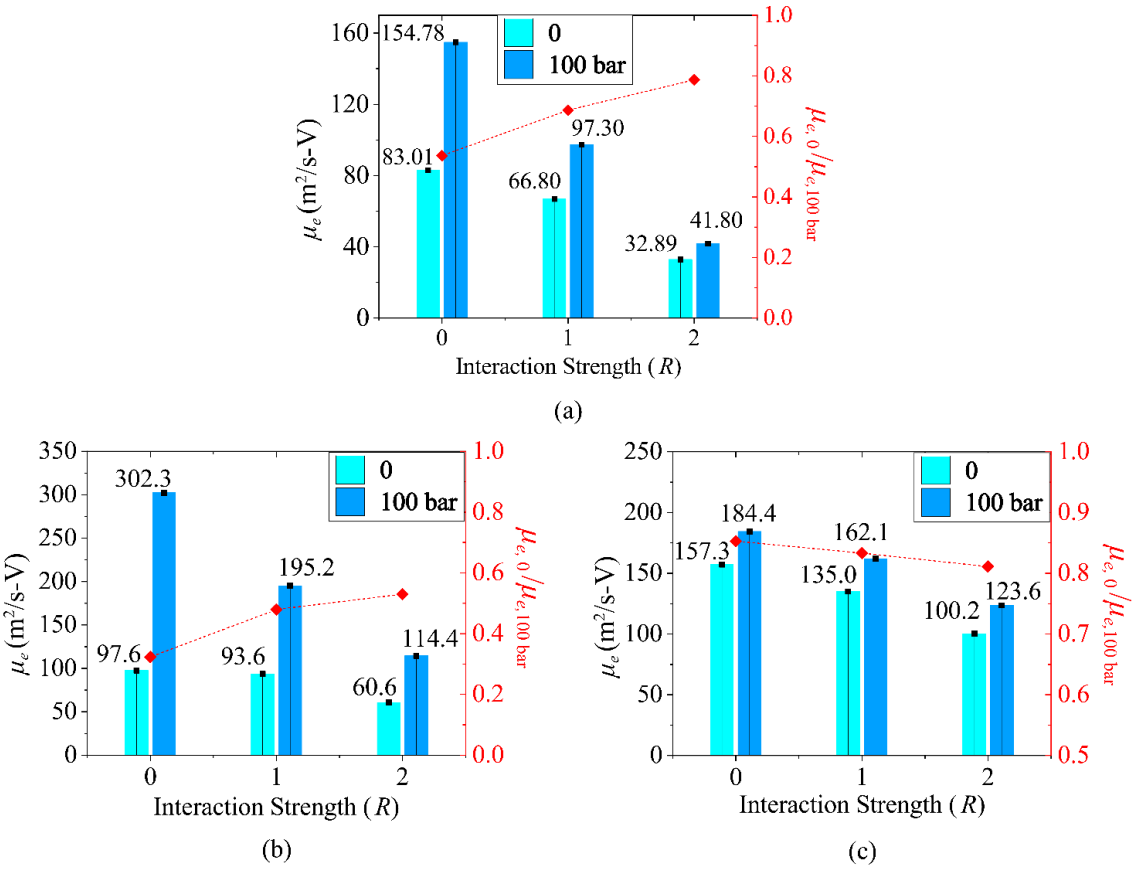

Figure 4.7 The mobility changing by coupling effect of different interaction strength at various temperature and channel size conditions. (a) T = 300 K, d = 14 Å, (b) T = 300 K, d = 40 Å, (c) T = 320 K, d = 14 Å.

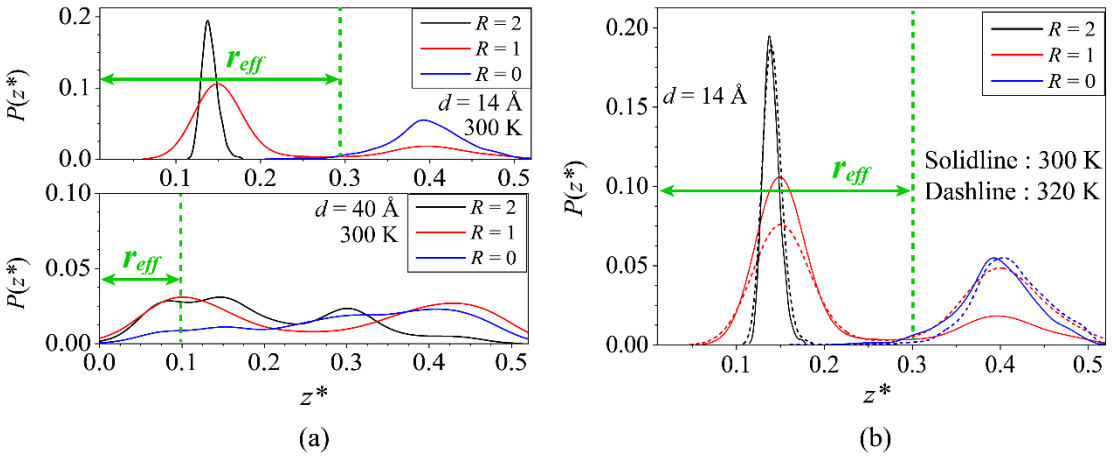

Figure 4.8 Distance distribution function between the ion and graphene wall from different interaction strength under (a) size difference, (b) temperature difference effect.

In contrast, the stronger surface interaction leads to the ion distribution closer to the channel wall with stronger resistance to the ion transport. When the channel size increases to 40 Å (Fig. 4.8a), the distance distribution from all interaction strengths extends across the channel. Therefore, ionic mobility significantly increases in all interaction strength conditions because the ion has less probability of being affected by surface interaction. In the case of $R = 0$, the least amount of the distribution inside the r_{eff} is observed in Fig. 4.8a. Thus, the ion transport with lower surface interaction has higher

On the other hand, when the temperature increases, the broadening of the distribution peak is observed, as shown in Fig. 4.8b. However, the ion with the highest surface interaction strength ($R = 2$) is still mostly distributed inside the r_{eff}. Since the surface interaction is the function of temperature, the sensitivity of ionic mobility on temperature increases with interaction strength.

The distance distribution of the ion with different surface interactions can also be used to discuss the coupling effect of ionic mobility. The study shows that the parabolic velocity profile not only appears at macroscopic channel flow but also exists inside the graphene nanochannel [49]. Therefore, when the ion is distributed near the center of the channel, the coupling effect from the convective flux is increased by higher flow velocity. Moreover, the larger channel size amplified the coupling effect because the distance distribution is more extended out of the effective range (r_{eff}). On the other hand, since the higher temperature raises the kinetics of all atoms in the system, the contribution of the surface

interaction and coupling effect from convective flux is reduced. Thus, the coupling effect on ionic mobility is decreased in higher temperature conditions.

4.6 Conclusions

The ion transport behaviors with different surface interactions were investigated through molecular dynamics simulation. The drift velocity of the ion shows a linear relationship with a relatively small electric field (< 100 mV/nm) or pressure difference (< 100 bar). The convective flux, which is driven by pressure difference, can alter the ionic mobility due to the coupling effect. The surface interaction changes the distance distribution between the ion and graphene wall. Therefore, the ionic mobility, either with or without the coupling effect from convective flux, is changed by interaction strength. A larger channel size increases the probability of the ion that leaves the effective range of the surface interaction. Thus, ionic mobility is increased with channel size. The channel size also affects the sensitivity of ionic mobility on surface interaction strength. The distance distribution function also indicates that the sensitivity of ionic mobility to temperature increases with surface strength. The parabolic velocity profile changes ionic mobility by coupling effect from convective flux. The coupling effect on ionic mobility is enhanced by larger channel size. However, the increment of the kinetic of the atoms from higher temperatures reduces the contribution of the coupling effect on ionic mobility. This study offers the perception of the ion transfer modifications, which have the potential application to the enhancement of the graphene electrodes.

Chapter 5
Summary and Future Work

5.1 Conclusions and Impacts

Through this Ph.D. research, several approaches to enhance the understanding of the synthesis and surface interaction of the graphene electrode with effective ion transport properties were demonstrated by multi-scale computational simulations. The water-ice interface propagation, a critical factor for the alignment of the graphene structure, was studied by microscale MD simulations and macroscale CFD simulations in Chapter 2 and Chapter 3, respectively. In Chapter 4, the surface interaction effect from graphene on the ion transport with convection flux was investigated. The conclusions and impacts of the presented research are summarized below:

- *Chapter 2: Microscopic mechanism of water-ice phase change and control.* For effective control of the directional graphene aerogel structure synthesized by freeze casting, the controlling mechanisms of water-ice interface propagation were examined using molecular dynamics simulations. This research showed that the maximum speed of ice propagation appears at 13 K of supercooling because of the competition between atomic mobility and thermodynamic driving force on phase change. Further analysis indicates that due to the different interfacial energy, ice propagation speed depends on the ice crystal orientation. Consequently, graphene-water surface interactions align ice clusters or graphene flakes to have a minimum energy state. Moreover, the basal plane of the ice crystal tends to be parallel with the graphene

surface, which suppresses ice propagation perpendicular to the graphene while enhancing in a parallel direction. Faster ice propagation in the in-plane direction reported in this research also explains the structuring mechanisms during freeze casting. In conclusion, this study shows that ice propagation and graphene structuring can be controlled at a microscopic level by managing the surface interaction and freezing temperature.

- *Chapter 3: Rayleigh-Bénard convection on the water-ice phase change.* This pioneering research aimed to investigate the interaction between the Rayleigh-Bénard convection and the water-ice phase changing via Computational Fluid Dynamics (CFD) simulation. This research demonstrated that the convection effect (Nusselt number) and interface propagation (freezing speed) have the opposite tendency with the density inverse parameter. Moreover, the higher inverse parameters intensify the interface propagation and simultaneously suppress the convection heat transfer. Therefore, the competition between the interface propagation and the convection effect leads to the largest surface height variation (σ_z) at an inverse parameter equal to the unity. On the other hand, the development of the convection circulation rolls is suppressed in low aspect ratio (Γ) conditions, which reduces the heat transfer and speeds up the ice propagation. Consequently, the opposite trend between convection and interface propagation with respect to Γ makes the maximum σ_z appears at 0.66 in Γ. In summary, the operating temperatures and the aspect ratio of the container during the freeze casting have significant effects on the ice propagation and the final casting products.

- *Chapter 4: Surface interaction effects of graphene on ion transport.* The ion transport behavior through the graphene channel under various operating and geometric conditions was investigated using molecular dynamics simulation. According to the simulation results, the drifting velocity of the ions has a linear relationship with the electric field when the field is low. Similar linear behavior was also observed in the ion transport driven by pressure difference. Furthermore, the electric mobility of the ion can also be raised by reducing interaction strength and increasing the channel size. However, it was observed that the electric mobility is coupled with external pressure difference (for convection), and with the coupling, ion transport by electric field can be more amplified under lower interaction strength, lower temperature, and smaller channel size. In the end, the changes in the ion transport and the coupling effect can be explained by the microscopic ion distribution function and hydraulic velocity profile. In conclusion, this study will provide a more comprehensive understanding of the pressure difference and electric-field coupling. Therefore, the findings from this research would potentially enable effective ion transport control inside the nanomaterials. Furthermore, the related applications, such as the organic redox flow battery, could also benefit from this study.

5.2 Recommendation for Future Studies

The following are the recommended future works for further understanding of water-ice phase change control and ion transport enhancement for performance improvement in graphene electrodes.

- **Microscopic mechanism of water-ice phase change and control.**

A couple of variables were investigated for a better understanding of water-ice interface propagation, such as temperature, crystal orientation, and surface interaction. However, the size effects on the water-ice interface propagation need further investigation to improve the simulation efficiency and accuracy. For example, the simulation result data from the smaller size will suffer from the noise, which increases the difficulty of the data analysis, and the oversized system would cause unnecessary consumption of the computing resources.

From the current research, the effect of temperature and surface interaction on the water-ice interface propagation is investigated. In future studies, the optimized freezing temperature for water-ice interface propagation with the interaction of graphene flakes is required to increase the efficiency of the graphene structuring.

In this research, the ice crystal orientation, which demonstrated that it can be changed by the graphene surface, affects the surface energy and the propagation of the water-ice interface. Therefore, the water-ice interface propagation speed under the influence of the surface interaction from graphene with different initial ice crystal orientations needs to be comprehensively studied.

- ***Rayleigh-Bénard convection on the water-ice phase change.***

In chapter 3, the ice surface was observed being changed by Rayleigh-Bénard convection. However, the Rayleigh number is expected to decrease since the characteristic length (L) will be reduced when the ice surface moves upward during freezing. Thus, a longer

simulation time is recommended to observe the variation of the ice surface difference with time.

In addition, the water-ice phase change under Rayleigh-Bénard convection with different concentrations of foreign objects is needed to examine the convection effect on the graphene structuring. Finally, further exanimation of the geometrical confinement effect on the interactions between the water-ice phase changing and convective heat transfer is needed to precisely control the variation of the water-ice interface.

- ***Surface interactions effect of graphene on the ion transport.***

The ion transfer properties under various operational and physical conditions were demonstrated in chapter 4. However, several important variables should be further investigated to enhance the understanding of ion transport behavior through the graphene nanostructure. For example, the ion concentration effect on the ion mobility coupling with convective flux undoubtedly needs to be further studied for more practical applications.

In addition, the surface treatment of graphene not only changes the graphene-ion interaction but also changes the interactions between graphene and water molecules. Thus, the sensitivity of ion mobility on different carbon-oxygen interaction strengths is needed for further investigation.

Finally, this work shows that reducing the surface interaction can increase ion mobility. However, the electrochemical redox reactions from the electrolyte can be suppressed simultaneously. Thus, optimized modification of the surface interaction of graphene is

needed to strike a balance between the ion transport efficiency and the electrochemical reaction rate of electrolytes inside the graphene electrode.

List of References

[1] B. Hu, C. DeBruler, Z. Rhodes, and T.L. Liu, Long-Cycling Aqueous Organic Redox Flow Battery (AORFB) toward Sustainable and Safe Energy Storage, *Journal of the American Chemical Society* 139 1207-1214 (3) 2017.

[2] K. Schmietendorf, J. Peinke, and O. Kamps, The impact of turbulent renewable energy production on power grid stability and quality, *The European Physical Journal B* 90 222 (11) 2017.

[3] A. Khan, S. Memon, and T.P. Sattar, Analyzing Integrated Renewable Energy and Smart-Grid Systems to Improve Voltage Quality and Harmonic Distortion Losses at Electric-Vehicle Charging Stations, *IEEE Access* 6 26404-26415 2018.

[4] P. Leung, X. Li, C. Ponce de León, L. Berlouis, C.T.J. Low, and F.C. Walsh, Progress in redox flow batteries, remaining challenges and their applications in energy storage, *RSC Advances* 2 10125-10156 (27) 2012.

[5] A.Z. Weber, M.M. Mench, J.P. Meyers, P.N. Ross, J.T. Gostick, and Q. Liu, Redox flow batteries: a review, *Journal of Applied Electrochemistry* 41 1137 (10) 2011.

[6] W. Wang, Q. Luo, B. Li, X. Wei, L. Li, and Z. Yang, Recent Progress in Redox Flow Battery Research and Development, *Advanced Functional Materials* 23 970-986 (8) 2013.

[7] M. Skyllas-Kazacos, M.H. Chakrabarti, S.A. Hajimolana, F.S. Mjalli, and M. Saleem, Progress in Flow Battery Research and Development, *Journal of The Electrochemical Society* 158 R55 (8) 2011.

[8] J. Noack, N. Roznyatovskaya, T. Herr, and P. Fischer, The Chemistry of Redox-Flow Batteries, *Angewandte Chemie International Edition* 54 9776-9809 (34) 2015.

[9] Z. Huang and A. Mu, Research and analysis of performance improvement of vanadium redox flow battery in microgrid: A technology review, *International journal of energy research* 45 14170-14193 (10) 2021.

[10] I. Aramendia, U. Fernandez-Gamiz, A. Martinez-San-Vicente, E. Zulueta, and J.M. Lopez-Guede, Vanadium Redox Flow Batteries: A Review Oriented to Fluid-Dynamic Optimization, *Energies (Basel)* 14 176 (1) 2020.

[11] R.P. Carvalho, C.F.N. Marchiori, D. Brandell, and C.M. Araujo, Tuning the Electrochemical Properties of Organic Battery Cathode Materials: Insights from Evolutionary Algorithm DFT Calculations, *ChemSusChem* 13 2402-2409 (9) 2020.

[12] R. Borah, F. Hughson, and T. Nann, Re-discovering micro-emulsion electrolytes: a biphasic electrolyte platform for Organic redox flow batteries,2021.

[13] X. Xing, Y. Huo, X. Wang, Y. Zhao, and Y. Li, A benzophenone-based anolyte for high energy density all-organic redox flow battery, *International Journal of Hydrogen Energy* 42 17488-17494 (27) 2017.

[14] T.B. Schon, B.T. McAllister, P.-F. Li, and D.S. Seferos, The rise of organic electrode materials for energy storage, *Chemical Society Reviews* 45 6345-6404 (22) 2016.

[15] J.A. Kowalski, L. Su, J.D. Milshtein, and F.R. Brushett, Recent advances in molecular engineering of redox active organic molecules for nonaqueous flow batteries, *Current Opinion in Chemical Engineering* 13 45-52 2016.

[16] J. Winsberg, T. Hagemann, T. Janoschka, M.D. Hager, and U.S. Schubert, Redox-Flow Batteries: From Metals to Organic Redox-Active Materials, *Angewandte Chemie International Edition* 56 686-711 (3) 2017.

[17] M. Park, J. Ryu, W. Wang, and J. Cho, Material design and engineering of next-generation flow-battery technologies, *Nature Reviews Materials* 2 16080 (1) 2016.

[18] X.W. Wu, T. Yamamura, S. Ohta, Q.X. Zhang, F.C. Lv, C.M. Liu, K. Shirasaki, I. Satoh, T. Shikama, D. Lu, and S.Q. Liu, Acceleration of the redox kinetics of VO2+/VO2+ and V3+/V2+ couples on carbon paper, *Journal of Applied Electrochemistry* 41 1183 (10) 2011.

[19] J. Li, J. Lai, J. Liu, R. Lei, and Y. Chen, Carbonized Dehydroascorbic Acid: Aim for Targeted Repair of Graphene Defects and Bridge Connection of Graphene Sheets with Small Size, *Nanomaterials (Basel, Switzerland)* 10 531 (3) 2020.

[20] W. Zhang, J. Xi, Z. Li, H. Zhou, L. Liu, Z. Wu, and X. Qiu, Electrochemical activation of graphite felt electrode for VO2+/VO2+ redox couple application, *Electrochimica Acta* 89 429-435 2013.

[21] J. Zhu, D. Yang, Z. Yin, Q. Yan, and H. Zhang, Graphene and Graphene-Based Materials for Energy Storage Applications, *Small* 10 3480-3498 (17) 2014.

[22] S. Deville, Freeze-casting of porous ceramics: A review of current achievements and issues, *Advanced Engineering Materials* 10 155-169 (3) 2008.

[23] Y.-K. Weng, A. Yousefzadi Nobakht, S. Shin, K.D. Kihm, and D.S. Aaron, Effects of mass and interaction mismatches on in-plane and cross-plane thermal transport of Si-doped graphene, *International Journal of Heat and Mass Transfer* 169 120979 2021.

[24] E.P. van der Poel, R.J.A.M. Stevens, and D. Lohse, Comparison between two- and three-dimensional Rayleigh–Bénard convection, *Journal of fluid mechanics* 736 177-194 2013.

[25] S. Hirano and C. Upper, Bacteria in the leaf ecosystem with emphasis on pseudomonas syringae-a pathogen, ice nucleus, and epiphyte, *Microbiology and Molecular Biology Reviews* 64 624-653 2000.

[26] T. Koop and B.J. Murray, A physically constrained classical description of the homogeneous nucleation of ice in water, *The Journal of Chemical Physics* 145 211915 (21) 2016.

[27] A. Michaelides and K. Morgenstern, Ice nanoclusters at hydrophobic metal surfaces, *Nature Materials* 6 597-601 (8) 2007.

[28] K.L. Scotti and D.C. Dunand, Freeze casting – A review of processing, microstructure and properties via the open data repository, FreezeCasting.net, *Progress in Materials Science* 94 243-305 2018.

[29] G. Shao, D.A.H. Hanaor, X. Shen, and A. Gurlo, Freeze casting: From low-dimensional building blocks to aligned porous structures—a review of novel materials, methods, and applications, *Advanced Materials* 32 1907176 (17) 2020.

[30] H. Bai, Y. Chen, B. Delattre, A.P. Tomsia, and R.O. Ritchie, Bioinspired large-scale aligned porous materials assembled with dual temperature gradients, *Science Advances* 1 e1500849 (11) 2015.

[31] H.-L. Gao, Y.-B. Zhu, L.-B. Mao, F.-C. Wang, X.-S. Luo, Y.-Y. Liu, Y. Lu, Z. Pan, J. Ge, W. Shen, Y.-R. Zheng, L. Xu, L.-J. Wang, W.-H. Xu, H.-A. Wu, and S.-H. Yu, Super-elastic and fatigue resistant carbon material with lamellar multi-arch microstructure, *Nature Communications* 7 12920 (1) 2016.

[32] M.C. Gutiérrez, Z.Y. García-Carvajal, M.J. Hortigüela, L. Yuste, F. Rojo, M.L. Ferrer, and F. del Monte, Biocompatible MWCNT scaffolds for immobilization and proliferation of E. coli, *Journal of Materials Chemistry* 17 2992-2995 (29) 2007.

[33] T. Zhai, X. Lu, H. Wang, G. Wang, T. Mathis, T. Liu, C. Li, Y. Tong, and Y. Li, An Electrochemical capacitor with applicable energy density of 7.4 Wh/kg at average power density of 3000 W/kg, *Nano Letters* 15 3189-3194 (5) 2015.

[34] A.Z. Lichtner, D. Jauffrès, C.L. Martin, and R.K. Bordia, Processing of hierarchical and anisotropic porosity LSM-YSZ composites, *Journal of the American Ceramic Society* 96 2745-2753 (9) 2013.

[35] V.C. Weiss, M. Rullich, C. Köhler, and T. Frauenheim, Kinetic aspects of the thermostatted growth of ice from supercooled water in simulations, *The Journal of Chemical Physics* 135 034701 (3) 2011.

[36] P. Montero de Hijes, J.R. Espinosa, C. Vega, and E. Sanz, Ice growth rate: Temperature dependence and effect of heat dissipation, *The Journal of Chemical Physics* 151 044509 (4) 2019.

[37] D. Rozmanov and P. Kusalik, Temperature dependence of crystal growth of hexagonal ice (I-h), *Physical Chemistry Chemical Physics : PCCP* 13 15501-15511 2011.

[38] J. Liu, C. Zhu, K. Liu, Y. Jiang, Y. Song, J. Francisco, Z. Cheng, and J. Wang, Distinct ice patterns on solid surfaces with various wettabilities, *Proceedings of the National Academy of Sciences* 114 11285-11290 (43) 2017.

[39] G. Algara-Siller, O. Lehtinen, F.C. Wang, R.R. Nair, U. Kaiser, H.A. Wu, A.K. Geim, and I.V. Grigorieva, Square ice in graphene nanocapillaries, *Nature* 519 443-445 (7544) 2015.

[40] A. Akaishi, T. Yonemaru, and J. Nakamura, Formation of water layers on graphene surfaces, *ACS Omega* 2 2184-2190 (5) 2017.

[41] S. Chen, A.P. Draude, A.X.C. Nie, H.P. Fang, N.R. Walet, S. Gao, and J.C. Li, Effect of layered water structures on the anomalous transport through nanoscale graphene channels, *Journal of Physics Communications* 2 085015 (8) 2018.

[42] J. Hayward and A. Haymet, The ice/water interface: Molecular dynamics simulations of the basal, prism, {20$\bar{2}$1}, and {2$\bar{1}$$\bar{1}$0} interfaces of ice Ih, *The Journal of Chemical Physics* 114 3713-3726 2001.

[43] Z. Gao, N. Giovambattista, and O. Sahin, Phase diagram of water confined by graphene, *Scientific Reports* 8 6228 (1) 2018.

[44] M. Matsumoto, S. Saito, and I. Ohmine, Molecular dynamics simulation of the ice nucleation and growth process leading to water freezing, *Nature* 416 409-413 (6879) 2002.

[45] J.L.F. Abascal, E. Sanz, R.G. Fernández, and C. Vega, A potential model for the study of ices and amorphous water: TIP4P/Ice, *The Journal of Chemical Physics* 122 234511 (23) 2005.

[46] J.-P. Ryckaert, G. Ciccotti, and H.J.C. Berendsen, Numerical integration of the cartesian equations of motion of a system with constraints: molecular dynamics of n-alkanes, *Journal of Computational Physics* 23 327-341 (3) 1977.

[47] R.W. Hockney and J.W. Eastwood, Computer Simulation Using Particles, 1st ed, *CRC Press,* 1988, pp. 367-304.

[48] L.S. Tee, S. Gotoh, and W.E. Stewart, Molecular parameters for normal fluids. Lennard-Jones 12-6 potential, *Industrial & Engineering Chemistry Fundamentals* 5 356-363 (3) 1966.

[49] D.C. Marable, S. Shin, and A. Yousefzadi Nobakht, Investigation into the microscopic mechanisms influencing convective heat transfer of water flow in graphene nanochannels, *International Journal of Heat and Mass Transfer* 109 28-39 2017.

[50] A. Kınacı, J.B. Haskins, C. Sevik, and T. Çağın, Thermal conductivity of BN-C nanostructures, *Physical Review B* 86 115410 (11) 2012.

[51] L. Verlet, Computer "Experiments" on classical fluids. I. Thermodynamical properties of Lennard-Jones molecules, *Physical Review* 159 98-103 (1) 1967.

[52] A. Tabazadeh, Y.S. Djikaev, and H. Reiss, Surface crystallization of supercooled water in clouds, *Proceedings of the National Academy of Sciences of the United States of America* 99 15873-15878 (25) 2002.

[53] Y. Lü, X. Zhang, and M. Chen, Size effect on nucleation rate for homogeneous crystallization of nanoscale water film, *The Journal of Physical Chemistry. B* 117 10241–10249 (35) 2013.

[54] P. Steinhardt, D. Nelson, and M. Ronchetti, Bond-orientational order in liquids and glasses, *Physical Review B* 28 784-805 (2) 1983.

[55] S. Auer and D. Frenkel, Advanced computer simulation: Approaches for soft matter sciences i, *Springer Berlin Heidelberg*, Berlin, Heidelberg, 2005, pp. 149-208.

[56] W. Lechner and C. Dellago, Accurate determination of crystal structures based on averaged local bond order parameters, *The Journal of Chemical Physics* 129 114707 (11) 2008.

[57] S. Javan Nikkhah, M.R. Moghbeli, and S.M. Hashemianzadeh, A molecular simulation study on the adhesion behavior of a functionalized polyethylene-functionalized graphene interface, *Physical Chemistry Chemical Physics* 17 27414-27427 (41) 2015.

[58] R.W. Zwanzig, High-temperature equation of state by a perturbation method. I. Nonpolar Gases, *The Journal of Chemical Physics* 22 1420-1426 (8) 1954.

[59] J. Wang, S. Shin, and A. Hu, Geometrical effects on sintering dynamics of Cu–Ag core–shell nanoparticles, *The Journal of Physical Chemistry C* 120 17791-17800 (31) 2016.

[60] M.A.A. Hasan, J. Wang, Y.C. Lim, A. Hu, and S. Shin, Concentration dependence of hydrogen diffusion in α-iron from atomistic perspectives, *International Journal of Hydrogen Energy* 44 27876-27884 (51) 2019.

[61] J. Key and D.W. Ball, Introductory Chemistry, 1st Canadian ed, *BCcampus,* 2014.

[62] Y. Zhang, E. Anim-Danso, S. Bekele, and A. Dhinojwala, Effect of surface energy on freezing temperature of water, *ACS Applied Materials & Interfaces* 8 17583-17590 (27) 2016.

[63] P. Virnau, F. Schmitz, and K. Binder, The ensemble switch method and related approaches to obtain interfacial free energies between coexisting phases from simulations: a brief review, *Molecular Simulation* 42 549-562 (6-7) 2016.

[64] R.A. Nistor, T.E. Markland, and B.J. Berne, Interface-limited growth of heterogeneously nucleated ice in supercooled water, *The Journal of Physical Chemistry B* 118 752-760 (3) 2014.

[65] T. Buttersack and S. Bauerecker, Critical radius of supercooled water droplets: On the transition toward dendritic freezing, *The Journal of Physical Chemistry B* 120 504-512 (3) 2016.

[66] T. Wang, Y. Lü, L. Ai, Y. Zhou, and M. Chen, Dendritic growth model involving interface kinetics for supercooled water, *Langmuir* 35 5162-5167 (15) 2019.

[67] S.-H. Guan, C. Shang, S.-D. Huang, and Z.-P. Liu, Two-stage solid-phase transition of cubic ice to hexagonal ice: Structural origin and kinetics, *The Journal of Physical Chemistry C* 122 29009-29016 (50) 2018.

[68] S. Mori and J. Zhang, Encyclopedia of Neuroscience, *Academic Press*, Oxford, 2009, pp. 531-538.

[69] W.S. Price, H. Ide, and Y. Arata, Self-diffusion of supercooled water to 238 K using PGSE NMR diffusion measurements, *The Journal of Physical Chemistry A* 103 448-450 (4) 1999.

[70] I.-C. Yeh and G. Hummer, System-size dependence of diffusion coefficients and viscosities from molecular dynamics simulations with periodic boundary conditions, *The Journal of Physical Chemistry B* 108 15873-15879 (40) 2004.

[71] M. Fitzner, G.C. Sosso, S.J. Cox, and A. Michaelides, The many faces of heterogeneous ice nucleation: Interplay between surface morphology and hydrophobicity, *Journal of the American Chemical Society* 137 13658-13669 (42) 2015.

[72] R.H. Henchman, Free energy of liquid water from a computer simulation via cell theory, *The Journal of Chemical Physics* 126 064504 (6) 2007.

[73] H.J.C. Berendsen, J.R. Grigera, and T.P. Straatsma, The missing term in effective pair potentials, *The Journal of Physical Chemistry* 91 6269-6271 (24) 1987.

[74] W. Wagner and A. Pruß, The IAPWS Formulation 1995 for the thermodynamic properties of ordinary water substance for general and scientific use, *Journal of Physical and Chemical Reference Data* 31 387-535 (2) 2002.

[75] C.-C. Cho, C.-L. Chen, and C.o.-K. Chen, Natural convection heat transfer performance in complex-wavy-wall enclosed cavity filled with nanofluid, *International Journal of Thermal Sciences* 60 255-263 2012.

[76] F.J. Arias and G.T. Parks, On the use of stimulated thermocapillary currents and virtual walls as computational tools for natural convection simulation in enclosed spaces, *International Journal of Thermal Sciences* 95 47-52 2015.

[77] O. kok seng, K. Osmond, and W. Tong, Reverse flow in natural convection heat pipe solar water heater, *International Journal of Low-Carbon Technologies* 10 2014.

[78] F.P. Incropera, Liquid cooling ofelectronic devices by sngle-phase convection, *Wiley,* 1999.

[79] J.C. Wyngaard, Atmospheric turbulence, *Annual Review of Fluid Mechanics* 24 205-234 (1) 1992.

[80] B. Stevens, Atmospheric moist convection, *Annual Review of Earth and Planetary Sciences* 33 605-643 (1) 2005.

[81] S.A. Thorpe, Recent developments in the study of ocean turbulence, *Annual Review of Earth and Planetary Sciences* 32 91-109 (1) 2004.

[82] G.-J. Huang, S.-C. Wong, and C.-P. Lin, Enhancement of natural convection heat transfer from horizontal rectangular fin arrays with perforations in fin base, *International Journal of Thermal Sciences* 84 164-174 2014.

[83] S.G. Taji, G.V. Parishwad, and N.K. Sane, Experimental investigation of heat transfer and flow pattern from heated horizontal rectangular fin array under natural convection, *Heat and Mass Transfer* 50 1005-1015 (7) 2014.

[84] F. Chillà and J. Schumacher, New perspectives in turbulent Rayleigh-Bénard convection, *The European Physical Journal E* 35 58 (7) 2012.

[85] S. Liu, L. Jiang, K.L. Chong, X. Zhu, Z.-H. Wan, R. Verzicco, R.J.A.M. Stevens, D. Lohse, and C. Sun, From Rayleigh–Bénard convection to porous-media convection: how porosity affects heat transfer and flow structure, *Journal of Fluid Mechanics* 895 A18 2020.

[86] E. Bodenschatz, W. Pesch, and G. Ahlers, Recent developments in Rayleigh-Bénard convection, *Annual review of fluid mechanics* 32 709-778 (1) 2000.

[87] S. Chandrasekhar, Hydrodynamic and hydromagnetic stability, *Clarendon Press,* Oxford,1961.

[88] P.G. Drazin and W.H. Reid, Hydrodynamic stability, 2nd ed. ed, *Cambridge University Press,* Cambridge,2004.

[89] C. Kanchana, Y. Su, and Y. Zhao, Regular and chaotic Rayleigh-Bénard convective motions in methanol and water, *Communications in Nonlinear Science and Numerical Simulation* 83 105129 2020.

[90] Y.-H. Yang, X. Zhu, B.-F. Wang, Y.-L. Liu, and Q. Zhou, Experimental investigation of turbulent Rayleigh-Bénard convection of water in a cylindrical cell: The Prandtl number effects for Pr > 1, *Physics of Fluids* 32 015101 (1) 2020.

[91] L. Valencia, J. Pallares, I. Cuesta, and F.X. Grau, Turbulent Rayleigh–Bénard convection of water in cubical cavities: A numerical and experimental study, *International Journal of Heat and Mass Transfer* 50 3203-3215 (15) 2007.

[92] G. Paolillo, C.S. Greco, T. Astarita, and G. Cardone, Experimental determination of the 3-D characteristic modes of turbulent Rayleigh–Bénard convection in a cylinder, *Journal of fluid mechanics* 922 2021.

[93] G.S. Kell, Density, thermal expansivity, and compressibility of liquid water from 0.deg. to 150.deg.. Correlations and tables for atmospheric pressure and saturation reviewed and expressed on 1968 temperature scale, *Journal of Chemical & Engineering Data* 20 97-105 (1) 1975.

[94] G. Ahlers, S. Grossmann, and D. Lohse, Heat transfer and large scale dynamics in turbulent Rayleigh-B'enard convection, *Reviews of Modern Physics* 81 503-537 (2) 2009.

[95] D. Lohse and K.-Q. Xia, Small-scale properties of turbulent Rayleigh-Bénard convection, *Annual Review of Fluid Mechanics* 42 335-364 2009.

[96] A. Xu, B.-R. Xu, L.-S. Jiang, and H.-D. Xi, Production and transport of vorticity in two-dimensional Rayleigh–Bénard convection cell, *Physics of Fluids* 34 013609 (1) 2022.

[97] J.-Y. Moon and B.-J. Chung, Time-dependent Rayleigh–Benard convection: Cell formation and Nusselt number, *Nuclear Engineering and Design* 274 146-153 2014.

[98] N.L. Francis, P.M. Hunger, A.E. Donius, U.G.K. Wegst, and M.A. Wheatley, Strategies for neurotrophin-3 and chondroitinase ABC release from freeze-cast chitosan–alginate nerve-guidance scaffolds, *Journal of Tissue Engineering and Regenerative Medicine* 11 285-294 (1) 2017.

[99] S. Deville, Freeze-casting of porous biomaterials: structure, properties and opportunities, *Materials* 3 1913-1927 (3) 2010.

[100] Y.-K. Weng, S. Shin, K.D. Kihm, M. Bahzad, and D.S. Aaron, Investigation of microscopic mechanisms for water-ice phase change propagation control, *International Journal of Heat and Mass Transfer* 184 122357 2022.

[101] P. Kumar, K. Srinivasan, and P. Dutta, Visualization of convection loops due to Rayleigh–Benard convection during solidification, *Mechanics Research Communications* 33 593-600 (5) 2006.

[102] O. Satbhai, S. Roy, S. Ghosh, S. Chakraborty, and R. Lakkaraju, Comparison of the quasi-steady-state heat transport in phase-change and classical Rayleigh-Bénard convection for a wide range of Stefan number and Rayleigh number, *Physics of fluids (1994)* 31 96605 (9) 2019.

[103] H. Jayakody, R. Al-Dadah, and S. Mahmoud, Computational fluid dynamics investigation on indirect contact freeze desalination, *Desalination* 420 21-33 2017.

[104] A.C. Bourdillon, P.G. Verdin, and C.P. Thompson, Numerical simulations of water freezing processes in cavities and cylindrical enclosures, *Applied Thermal Engineering* 75 839-855 2015.

[105] ANSYS® FLUENT. 2021, *ANSYS, Inc.*: Canonsburg, Pennsylvania.

[106] R.C. Weast and M.J. Astle, CRC Handbook of Chemistry and Physics. 1982, *CRC Press, Boca Raton, Florida*.

[107] G. Silano, K. Sreenivasan, and R. Verzicco, Numerical simulations of Rayleigh–Bénard convection for Prandtl numbers between 10^1 and 10^4 and Rayleigh numbers between 10^5 and 10^9, *Journal of Fluid Mechanics* 662 409-446 2010.

[108] T. Hartlep, A. Tilgner, and F.H. Busse, Large scale structures in Rayleigh-B'enard convection at high Rayleigh numbers, *Physical Review Letters* 91 064501 (6) 2003.

[109] K.R. Rajagopal, G. Saccomandi, and L. Vergori, Stability analysis of the Rayleigh–Bénard convection for a fluid with temperature and pressure dependent viscosity, *Zeitschrift für angewandte Mathematik und Physik* 60 739-755 (4) 2009.

[110] H.R. Upadhye and S.G. Kandlikar. Optimization of microchannel geometry for direct chip cooling using single phase heat transfer. in *ASME 2004 2nd International Conference on Microchannels and Minichannels*. 2004.

[111] S. Wagner and O. Shishkina, Aspect-ratio dependency of Rayleigh-Bénard convection in box-shaped containers, *Physics of Fluids* 25 085110 (8) 2013.

[112] W.P. Jones and B.E. Launder, The prediction of laminarization with a two-equation model of turbulence, *International Journal of Heat and Mass Transfer* 15 301-314 (2) 1972.

[113] S.V. Patankar, Numerical heat transfer and fluid flow, *Taylor & Francis.,* 1980.

[114] U. Roy and P.K. Roy, Advanced Analytic and Control Techniques for Thermal Systems with Heat Exchangers, *Academic Press*, 2020, pp. 197-207.

[115] V. Kumar, M. Kumawat, A. Srivastava, and S. Karagadde, Mechanism of flow reversal during solidification of an anomalous liquid, *Physics of Fluids* 29 123603 (12) 2017.

[116] R.S. Tankin and R. Farhadieh, Effects of thermal convection currents on formation of ice, *International Journal of Heat and Mass Transfer* 14 953-961 (7) 1971.

[117] X.-J. Huang, Y.-R. Li, L. Zhang, and C.-M. Wu, Turbulent Rayleigh-Bénard convection of cold water near its maximum density in a vertical cylindrical container, *International Journal of Heat and Mass Transfer* 116 185-193 2018.

[118] E. Koschmieder and C.D. Andereck, Bénard cells and Taylor vortices, *Cambridge University Press,* 1993.

[119] M.J. Richardson and R.W. Kallen, Contextuality from Quantum Physics to Psychology, pp. 229-286.

[120] P. Manneville, Dynamics of Spatio-Temporal Cellular Structures: Henri Bénard Centenary Review, *Springer New York*, New York, NY, 2006, pp. 41-65.

[121] W.H. Leong, K.G.T. Hollands, and A.p. Brunger, Experimental Nusselt numbers for a cubical-cavity benchmark problem in natural convection, *International Journal of Heat and Mass Transfer* 42 1979-1989 (11) 1999.

[122] H. Li, Z. Song, X. Zhang, Y. Huang, S. Li, Y. Mao, H.J. Ploehn, Y. Bao, and M. Yu, Ultrathin, molecular-sieving graphene oxide membranes for selective hydrogen separation, *Science* 342 95-8 (6154) 2013.

[123] M. Lozada-Hidalgo, S. Hu, O. Marshall, A. Mishchenko, A.N. Grigorenko, R.A. Dryfe, B. Radha, I.V. Grigorieva, and A.K. Geim, Sieving hydrogen isotopes through two-dimensional crystals, *Science* 351 68-70 (6268) 2016.

[124] M. Hu and B. Mi, Enabling Graphene Oxide Nanosheets as Water Separation Membranes, *Environmental Science & Technology* 47 3715-3723 (8) 2013.

[125] B. Mi, Graphene Oxide Membranes for Ionic and Molecular Sieving, *Science* 343 740-742 (6172) 2014.

[126] T. Shigematsu, Redox flow battery for energy storage, *SEI technical review* 73 13 (7) 2011.

[127] K.S. Novoselov, Nobel Lecture: Graphene: Materials in the Flatland, *Reviews of Modern Physics* 83 837-849 (3) 2011.

[128] K. Nomura and A.H. MacDonald, Quantum Hall Ferromagnetism in Graphene, *Physical Review Letters* 96 256602 (25) 2006.

[129] A.A. Balandin, Thermal properties of graphene and nanostructured carbon materials, *Nature Materials* 10 569-581 (8) 2011.

[130] A. Ashraf, Y. Wu, M.C. Wang, K. Yong, T. Sun, Y. Jing, R.T. Haasch, N.R. Aluru, and S. Nam, Doping-Induced Tunable Wettability and Adhesion of Graphene, *Nano Letters* 16 4708-4712 (7) 2016.

[131] T. Van Khai, H.G. Na, D.S. Kwak, Y.J. Kwon, H. Ham, K.B. Shim, and H.W. Kim, Significant enhancement of blue emission and electrical conductivity of N-doped graphene, *Journal of Materials Chemistry* 22 17992-18003 (34) 2012.

[132] E. Yusko, Y. Billeh, and M. Mayer, Current oscillations generated by precipitate formation in the mixing zone between two solutions inside a nanopore, *Journal of physics. Condensed matter : an Institute of Physics journal* 22 454127 2010.

[133] Y. Roy, D.M. Warsinger, and J.H. Lienhard, Effect of temperature on ion transport in nanofiltration membranes: Diffusion, convection and electromigration, *Desalination* 420 241-257 2017.

[134] J. Kong, Z. Bo, H. Yang, J. Yang, X. Shuai, J. Yan, and K. Cen, Temperature dependence of ion diffusion coefficients in NaCl electrolyte confined within graphene nanochannels, *Physical Chemistry Chemical Physics* 19 7678-7688 (11) 2017.

[135] K. Guan, Y. Jia, Y. Lin, S. Wang, and H. Matsuyama, Chemically Converted Graphene Nanosheets for the Construction of Ion-Exclusion Nanochannel Membranes, *Nano Letters* 21 3495-3502 (8) 2021.

[136] Q. Xie, M.A. Alibakhshi, S. Jiao, Z. Xu, M. Hempel, J. Kong, H.G. Park, and C. Duan, Fast water transport in graphene nanofluidic channels, *Nature Nanotechnology* 13 238-245 (3) 2018.

[137] F. Sofos, T.E. Karakasidis, and D. Spetsiotis, Molecular dynamics simulations of ion separation in nano-channel water flows using an electric field, *Molecular Simulation* 45 1395-1402 (17) 2019.

[138] N. Modi, M. Winterhalter, and U. Kleinekathöfer, Computational modeling of ion transport through nanopores, *Nanoscale* 4 6166-6180 (20) 2012.

[139] A.-E. Ailenei and T.A. Beu, Ion transport through gated carbon nanotubes: Molecular dynamics simulations using polarizable water, *Journal of Molecular Structure* 1245 131022 2021.

[140] T.A. Beu, Molecular dynamics simulations of ion transport through carbon nanotubes. III. Influence of the nanotube radius, solute concentration, and applied electric fields on the transport properties, *The Journal of Chemical Physics* 135 044516 (4) 2011.

[141] S. Plimpton, Fast Parallel Algorithms for Short-Range Molecular Dynamics, *Journal of Computational Physics* 117 1-19 (1) 1995.

[142] Y. Yu, J. Fan, A. Esfandiar, Y. Zhu, H. Wu, and F. Wang, Charge Asymmetry Effect in Ion Transport through Angstrom-Scale Channels, *The Journal of Physical Chemistry C* 123 1462-1469 (2) 2019.

[143] Y. Jin, T. Ng, R. Tao, S. Luo, Y. Su, and Z. Li, Coupling effects in electromechanical ion transport in graphene nanochannels, *Physical Review E* 102 033112 (3) 2020.

Vita

Yu-Kai Weng (hn12035545@gmail.com) was born in September in Taipei, Taiwan, in 1987. He graduated with a Bachelor of Science in June of 2010 from National Cheng Kung University, with a major in Aeronautics and Astronautics, and a Master of Science with a major in Aerospace Engineering from Georgia Institute of Technology in May of 2013. He came to the University of Tennessee for his Ph.D. in January of 2016 and started his research with the multi-scale simulation of heat and mass transfer in Dr. Seungha Shin's group in 2018. His graduate study was supported by Dr. Seungha Shin.